
University of Padova

The Ph.D. School on Information Engineering

Department of Information Engineering


# A Unified Framework For Blood Data Modeling In Dynamic Positron Emission Tomography Studies

PhD Thesis


**MATTEO TONIETTO**

**Supervisor:** Alessandra Bertoldo
Professor



Padova, November 2016

# Abstract

Quantification of dynamic PET images requires the measurement of radioligand concentrations in the arterial plasma. In general, this cannot be derived from PET images directly but it must be measured from blood samples taken from the subject's radial artery. The accurate measurement of parent radioligand concentration in plasma is a major challenge due to the presence of radiometabolites, i.e. molecules produced from the breakdown of the tracer in the organism which still contain the radioactive isotope and that are found in plasma.

Through the application of radiochromatographic techniques, it is possible to separate the contribute of the radiometabolites by measuring the fraction of unchanged tracer over the total activity, the Parent Plasma fraction. However, these measurements can only be performed on a subset of the plasma samples due to the fast decay of the radioactivity. Therefore, the parent fraction measurements must be fitted with a mathematical model to interpolate the missing values.

One key assumption of the tissue kinetic model is that the input function is fully known and not affected by measurement error. Instead, after correcting for the presence of radiometabolites, the resulting input function consists of noisy and discrete samples. Consequently, a mathematical model is fit to the plasma data to obtain a continuous and noise-free description.

In summary one has to apply at least two models to arrive at the final input function: one for the parent plasma fraction and one for the input function.

The models currently used in literature are just empirical functions chosen with the unique purpose of describing the data. They do not explicitly consider the underlying physiologic processes of radioligand metabolism (e.g., the rate of metabolism) or experiment variables (e.g., radioligand injection time).

The aim of this thesis was to develop and validate a unified framework for the plasma data modeling, which was both biologically and experimentally informed,

in order to achieve a better description of the plasma data. Moreover, an estimation algorithm was also proposed which was able to adapt the complexity of the models to the data available (manual versus automatic samples) exploiting basis pursuit techniques already applied in PET. Furthermore, the algorithm was designed to require minimal interaction from the user as most of initial parameters are derived from the data itself.

Initially, a technique to include the duration of radioligand injection in any of the existing parent plasma fraction model was developed to achieve a more accurate description of the plasma measurements. This new formulation (here called convoluted model) was tested on three datasets with different parent kinetics: [$^{11}$C]NOP-1A, [$^{11}$C]MePPEP, and [$^{11}$C](*R*)-rolipram. Results showed that convoluted models better described the fraction of unchanged parent in the plasma compared with standard models for all three datasets (weighted residuals sum of squares up to 25% lower).

Subsequently, this approach was extended also for the model of the input function. Instead of applying it directly to the standard input function models as for the parent plasma fraction, a new formulation was derived from the tracer-tracee theory to describe the kinetic of the parent in plasma. The resulting input function model was therefore based on physiological assumptions and it accounted for the injection duration. This was compared against the standard models on eight different datasets acquired from different PET facilities. The physiological model provided a better fit of the noisy input function data in all the dataset considered, as measured by the Akaike Information index (up to 61% lower for the physiological model).

In the final part, the tracer-tracee theory was applied also for the radiometabolite model. Moreover, a completely automatic pipeline for the plasma data modeling was developed. This pipeline takes the raw plasma measurement as input and returns a modeled input function ready to be used for tissue quantification. The pipeline was tested on four different tracers ([$^{11}$C]PBR28, [$^{11}$C]MePPEP, [$^{11}$C]WAY-100635 and [$^{11}$C]PiB) with automatic and manual blood sampling. The input function estimated with it was shown to provide a better fit (weighted residuals sum of squares up to 14% lower) of the tissue time activity curves in three of the four datasets (for [$^{11}$C]PBR28 the difference was not significant) compared to the standard input function.

The final result of this thesis consists in a pipeline for the automatic fit of the plasma data with physiologically and experimentally informed models.

## Keywords

Positron Emission Tomography, PET, Arterial Input Function, Radiometabolites correction, Kinetic modeling, Tracer

# Contents

# Preface

All of the work presented henceforth was conducted in the Functional and Anatomical Imaging Research group at the Department of Information Engineering, University of Padova, Italy during a 3 years PhD program on Bioengineering.

Part of the introduction has been published as a review on radiometabolite correction in the Journal of Cerebral Blood Flow and Metabolism (Tonietto, M., Rizzo, G., Veronese, M., Fujita, M., Zoghbi, S. S., Zanotti-Fregonara, P., and Bertoldo, A. Plasma radiometabolite correction in dynamic PET studies: Insights on the available modeling approaches, J. Cereb. Blood Flow Metab 36(2), 326–339. http://doi.org/10.1177/0271678X15610585, 2016).

A version of Chapter 2 has been published as (Tonietto, M., Veronese, M., Rizzo, G., Zanotti-Fregonara, P., Lohith, T. G., Fujita, M., ... Bertoldo, A. Improved models for plasma radiometabolite correction and their impact on kinetic quantification in PET studies. J. Cereb. Blood Flow Metab 35(9), 1462–1469. http://doi.org/10.1038/jcbfm.2015.61, 2015).

A version of the material contained in Chapter 3 has been published as a short paper as (Tonietto, M., Rizzo, G., Veronese, M., and Bertoldo. Modelling arterial input functions in positron emission tomography dynamic studies. In 2015 37th Annual International Conference of the IEEE Engineering in Medicine and Biology Society (EMBC) (pp. 2247–2250). IEEE. http://doi.org/10.1109/EMBC.2015.7318839, 2015).

A preliminary form of Chapter 4 was presented at the Eleventh International Symposium on Functional Neuroreceptor Mapping of the Living Brain, (NeuroReceptor Mapping 2016), Boston (MA, USA) and a manuscript is currently under preparation.

Finally, appendices contain the mathematical derivations that support most of the results obtained in this work and they mostly consist in original material.

I was responsible for all major areas of concept formation and data analysis, as well as the majority of manuscripts composition. None of the data used were collected in Padova but they have been kindly shared by several institutions worldwide such as the Molecular Imaging Branch of the National Institute of mental Health, USA; the Section on Neuroadaptation and Protein Metabolism of National Institute of mental Health, USA; the PET Research Center, University of Pittsburgh, USA; the Department of Radiology, Columbia University, USA; Institute of Psychiatry, Psychology and Neuroscience, King's College,UK.

Chapter 1

# Introduction

Positron Emission Tomography (PET) allows to image the biodistribution and kinetics of radiopharmaceuticals in brain with great accuracy and minimum invasiveness [1]. Radiopharmaceuticals are chemical compounds in which one or more atoms have been replaced by a radioisotope. This leaves the chemical proprieties of the molecule unchanged so that, by virtue of the radioactive decay, this can be used as a tracer in conjunction with a PET scanner. In fact, once injected into the organism, the radiocompound will have the same metabolic behavior as the substance being traced (denoted as tracee). Moreover, radiolabeled tracers can be produced with high specific activity, allowing the experimenter to inject small tracer amounts (few nanomoles), thereby avoiding any unwanted pharmacological effect [2].

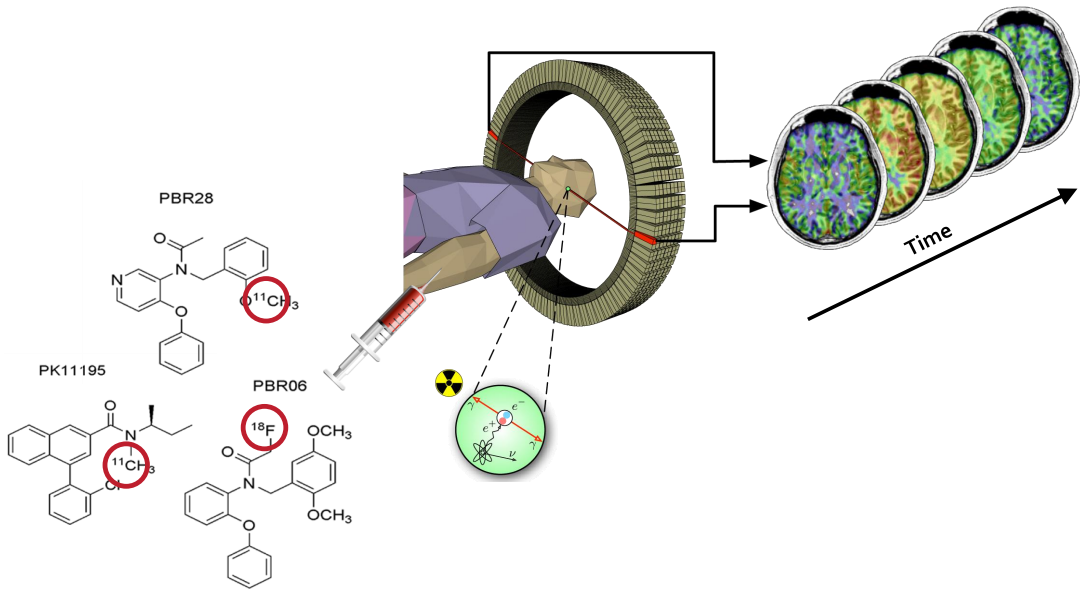


Figure 1.1: *Figure schematizes a typical dynamic brain PET experiment: from left to right one of the chemical compound, in which one atom has been replaced by a radioisotope (red circle), is injected intravenously at the beginning of the PET acquisition, obtaining dynamic images of the tracer concentration in brain.*

Indeed, a PET radiolabeled agent must meet the requirements of being an ideal tracer: it must be detectable by an observer; its introduction into a system must not perturb the system being studied (i.e. the amount of tracer is very small compared with the amount of tracee), and it must be indistinguishable with respect to the properties of the tracee system being studied [3].

Dynamic PET exams produce three-dimensional images throughout the duration of the experiment, starting from the injection of the tracer into the subject venous system. With reconstruction algorithm and corrections for the physical effects such as attenuation and scatter, quantitatively accurate measurements of regional radioactivity concentration can be obtained [4].

Interpreting these data by means of specific mathematical models can improve the kind and quality of information that can be extracted allowing the quantification of various physiological parameters. These includes enzymatic rates, perfusion, protein synthesis or binding potential, accordingly to the tracer employed [5]. This information can be used to monitor the progress of neurological diseases or to assess the effects of specific drugs, such as their penetration into target sites, their binding to specific receptors and their effects on the metabolic processes [6].

Since PET tracers can be assumed as ideal tracers, they can be studied through the framework of compartmental modeling. Although several of such compartmental models have been proposed, based on different assumptions and with various degrees of complexity and biological plausibility, they all describes the kinetic of the tracer concentration in the tissue, $C_T$, which correspond to what the PET scanner measures. However, to estimate the parameters of these models, it is necessary to know also the input of the system, that is the concentration of the tracer in the arterial plasma, which is known as the arterial input function or the parent concentration $C_p$.

In general, this cannot be derived from PET images directly but it must be measured from blood samples taken from the subject's radial artery. An accurate measurement of the input function is an essential step for PET images quantification as this represents the forcing function of the tissue compartmental model, substantially driving the kinetic estimation process. In compartmental models the forcing function is assumed to be known without measurement error, thus any inaccuracy present in the input function will be translated in a bias of the tissue parameter estimates.

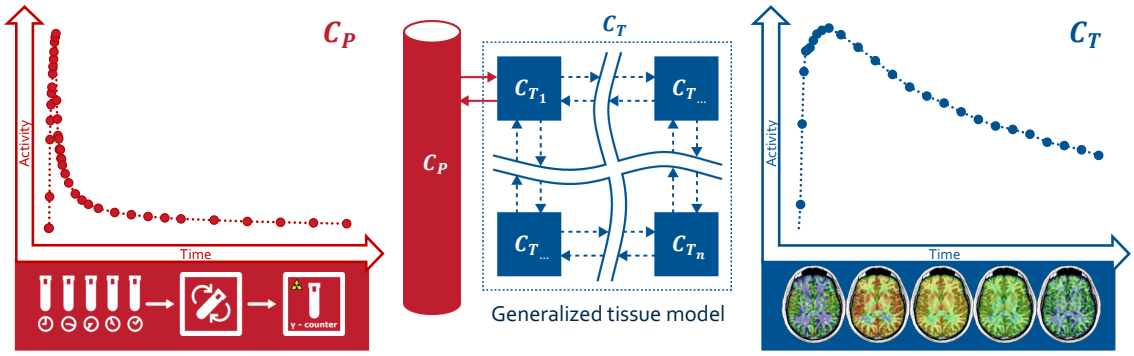


Figure 1.2: *Figure shows the three ingredients for the kinetic analysis of PET images: the arterial input function (left), the kinetic model (middle) and the PET images (right).*

## 1.1 Notation

In this thesis the following notation will be used to indicate discrete values (measured or derived):

- $C_b$ is the whole blood concentration;
- $C_{tot}$ is the total concentration in plasma (either free or bound to plasma protein);
- $POB$ is the Plasma-Over-Blood ratio
- $PPf$ is the Plasma Parent fraction;
- $C_p$ is the parent concentration in plasma, i.e. the input function;
- $C_{met}$ is the radiometabolite(s) concentration in plasma.

The same variables with the prefix $y$ will indicate their time-continuous model description, i.e. $yC_{tot}$, $yPOB$, $yPPf$, $yC_p$, $yC_{met}$; the prefix $w$ will indicate the weights used for data fitting, specifically , i.e. $wC_{tot}$, $wPPf$, $wC_p$, $wC_{met}$.

## 1.2 Measuring the input function

The accurate measurement of parent radioligand concentration in plasma is a major challenge of quantitative PET imaging. Radiolabeled compounds injected into the blood stream are exposed to a complex and unpredictable chemical environment and thus may break down in one or more metabolites. At least one of these metabolites would contain the radioisotope and is therefore named radiometabolite. To correctly quantify the binding of a radioligand, the amount of

radiometabolites should be taken into account [7]. Depending on the chemical characteristics of the radiometabolites and on the transport mechanism between blood and tissue, the radiometabolites may remain confined to the vascular compartment, migrate into the tissue along with the parent radioligand or even be created inside the tissue. Radiometabolites are often less lipophilic than their parent, and therefore are less likely to cross the blood–brain barrier and enter the brain. Thus, if the radiometabolites are confined to the blood compartment, only the concentration of parent radioligand should be used as input for modeling the tissue kinetics. By contrast, radiometabolites that cross the blood–brain barrier or originate directly inside the tissue [8] must be incorporated into the model as a second input or as an additional compartment, respectively.

Serial arterial blood samples are usually drawn during the PET scan, in order to assess the concentration of parent radioligand over time. Blood samples may be drawn manually or with an automated blood sampling system equipped with an online detector or with a fraction collector. The online detector allows the best definition of the peak, by continuously measuring arterial whole-blood concentrations. However, some manual blood samples are still required to obtain the plasma concentration and to separate the parent from its radiometabolites. The fraction collector instead provides discrete blood measurements as in the manual sampling, but with a higher frequency and more precise timing.

The first quantity usually measured is the whole blood concentration $C_b$, which is obtained by inserting the blood sample into a gamma counter or directly from the online detector. However, $C_b$ includes the contribute of the blood cells, while only the tracer in plasma is available for tissue exchange. Nevertheless, $C_b$ is still measured for the blood volume correction in the tissue models.

Plasma is subsequently separated from blood cells by means of a centrifuge and its total activity $C_{tot}$ is measured again with a gamma counter. In case the automated blood sampling system was employed, the values of $C_{tot}$ would be known only on few manual samples. The common practice to obtain the $C_{tot}$ values for the other time points is to compute the Plasma Over Blood (*POB*) ratio as:

$$POB(t) = \frac{C_{tot}(t)}{C_b(t)} \tag{1.1}$$

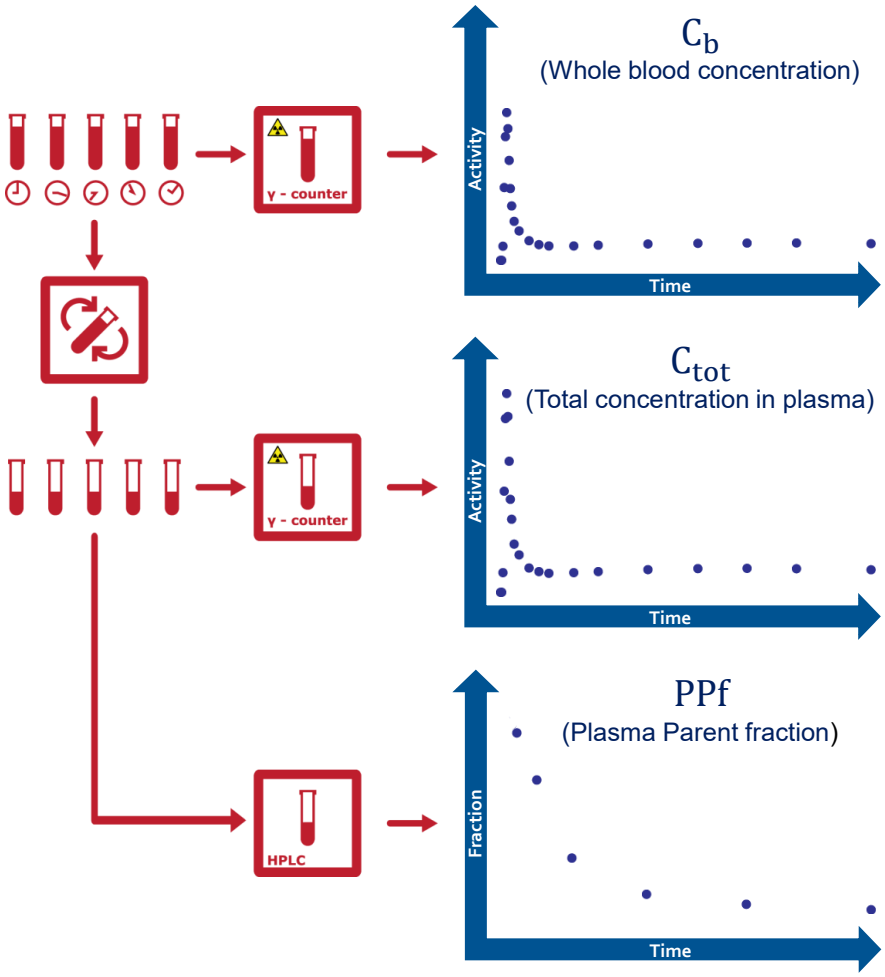


Figure 1.3: *Blood samples processing: (top) blood samples are drawn at various time points and their radioactivity is measured with a gamma counter obtaining the whole blood activity - $C_b$. (Middle) The samples are then centrifuged to separate the blood cells from plasma and the total activity in plasma - $C_{tot}$ - is measured again with the gamma counter. (Bottom) The HPLC measures the fraction of activity due to the parent in plasma - PPf*

and fit a mathematical function, *yPOB*, to it. The full time course of $C_{tot}$ is then estimated as:

$$C_{tot}(t) = C_b(t) \cdot yPOB(t) \tag{1.2}$$

Several choices are available for the form of *yPOB*, from polynomial to exponential functions. However, how much this choice affects the tissue estimates has never been carefully investigated. Notably, this step is necessary only when the online detector is employed.

The fraction of unchanged radioligand in plasma (the Plasma Parent fraction or *PPf*) is measured with techniques such as high-performance liquid chromatogra-

phy (HPLC), thin layer chromatography or other chromatographic methods. Since radiometabolites are usually less lipophilic than the parent, they elute earlier on HPLC. Thus, an online radiation detector attached to the HPLC will first measures the peak(s) of activity related to the radiometabolites and then the peak of activity related to parent (Figure 1.4). The value of the *PPf* at time $t$ ($PPf(t)$) is hence calculated as the ratio of the area under the curve of the parent peak ($AUC_p(t)$) and the total area ($AUC_{tot}(t)$) in the radiochromatogram:

$$PPf(t) = \frac{AUC_p(t)}{AUC_{tot}(t)} = \frac{AUC_p(t)}{AUC_p(t) + AUC_{met}(t)} \tag{1.3}$$

where $AUC_{met}$ is the area under the curve of the radiometabolites peak(s).

The fast decay of radioactivity, especially with $^{11}$C-labeled tracer, limits the total number of samples that can be analyzed by chromatography. Therefore, for kinetic modeling, *PPf* data points are generally fitted with a mathematical function, with the purpose of obtaining a smooth and continuous *yPPf* curve from a series of discrete noisy samples. Although *PPf* measurements are sometimes linearly interpolated [10][11] the use of a model is preferable to minimize the impact of measurement errors [12].The input function is then calculated as:

$$C_p(t) = C_{tot}(t) \cdot yPPf(t) \tag{1.4}$$

The choice of the *yPPf* model is a crucial step for kinetic modeling. Indeed, a carefully selected *yPPf* model allowed Parsey and colleagues [13] to nearly halve the retest variability of the total volume of distribution ($V_T$) of [$^{11}$C]DASB compared to the results obtained with the *yPPf* model commonly used in the literature. Furthermore, Wu and colleagues [14] showed that different models can lead to significant differences in both binding potential ($BP$) and $V_T$ quantification of [$^{11}$C]WAY-100635.

Since the tissue models assume that the input function is not affected by measurement noise and to obtain a continuous curve necessary for the numerical integrations involved in such models, also the input function is fitted with a model ($yC_p$), generating a continuous and noise-free curve. In summary, once the total tracer activity in plasma is known one has to apply at least two models to arrive at the final input function: one for *PPf* and one for $C_p$.

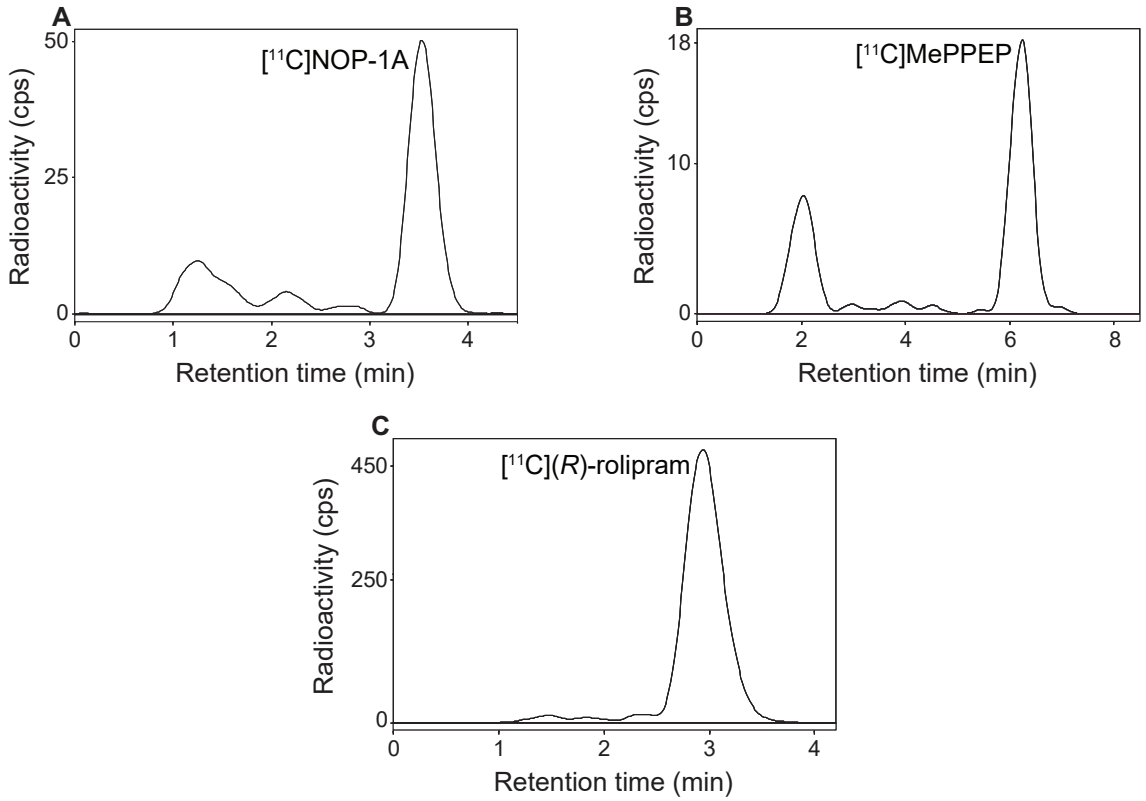


Figure 1.4: *Figure show the radiochromatograms derived from the HPLC analysis of: A) Human plasma sample at 10 min after the intravenous injection of [$^{11}$C]NOP-1A (733 MBq). There are at least four radiometabolites A and B = 22.1%; C = 6.5%; D = 2.4%; and parent = 69%. The parent radioligand eluted at 3.55 min and was well separated from the rest of the radiometabolites. B) Human plasma sample at 10 min after the intravenous injection of [$^{11}$C]MePPEP (625 MBq). There are at least five radiometabolites A = 29.6%; B = 2.0%; C = 3%; D = 18.8%; and parent = 62.6%. The parent radioligand eluted at 6.37 min and was well separated from the rest of the radiometabolites. C) Human plasma sample at 6 min after the intravenous injection of [$^{11}$C](R)-rolipram (744 MBq). There are three radiometabolites A = 2.34%; B = 1.42%; C = 2.05%; and parent = 94.2%. The parent radioligand eluted at 2.95 min and was well separated from the rest of the radiometabolites. All the radio analysis were done according to methodology detailed in [9].*

## 1.3 Modeling the Plasma Parent fraction

The model *yPPf* reflects the *PPf* properties: its value may range from 1 to 0, where 1 means that all radioactivity measured from the plasma sample is due to the unchanged radioligand and 0 that the radioligand has been completely metabolized. The *PPf* curve has usually an initial value of 1 and then decreases monotonically and sigmoidally toward 0. However, different shapes are possible. For example, the parent fraction of [$^{11}$C]DASB displays an initial rising phase [13] probably because the parent, but not the radiometabolites, is trapped in the

lungs. The majority of *yPPf* models can be categorized into three main classes: Power models, Hill models and Exponential models:

**Power models**

First proposed by Watabe and colleagues [15] for [$^{11}$C]MDL 100,907 and then extended by both Meyers and colleagues [16] for [$^{18}$F]CPFPX and by Hinz and colleagues [17] for [$^{11}$C]MDL 100,907 again, Power models are characterized by the following general expression:

$$yPPf(t) = \frac{1}{[1 + (a \cdot t)^b]^c} \tag{1.5}$$

with $a > 0$, $b > 1$ and $c > 0$. This model is characterized by a sigmoidal shape that starts from 1 with a zero first derivative and then approaches 0 for $t \to \infty$. For $0 < b \leq 1$, the model becomes a convex function.

**Hill models**

A Hill function was firstly used by Gunn and colleagues [18] to describe the radiometabolite fraction of [$^{11}$C]WAY-100635. This model was subsequently used to fit the *PPf* kinetic of many different radioligands such as (*R*)-[$^{11}$C]Verapamil [19], [$^{11}$C]flumazenil [20] or [$^{11}$C]NOP-1A [21]. A general expression for the Hill model is given by:

$$yPPf(t) = 1 + \frac{(a-1) \cdot t^b}{c + t^b} \tag{1.6}$$

with $0 \leq a < 1$, $b > 0$ and $c > 0$. The shape of the model is again sigmoidal, but for $t \to \infty$ tends to $a$ instead of zero. This allows a better description of radiotracers whose plasma concentration shows a plateau. An extension of the Hill model was presented by Asselin end colleagues [22] for [$^{11}$C]FLB457 and then used for[$^{11}$C]PiB [23] and [$^{18}$F]FLT [24]. Its formulation is

$$yPPf(t) = 1 + \frac{[(a-1) - d \cdot t] \cdot t^b}{c + t^b} \tag{1.7}$$

Compared to equation 1.6, this formulation presents one extra parameter $d$, which makes the model decrease toward an oblique asymptote whose slope equals $-d$. This variation of the Hill model is thus suited for radioligands which are rapidly metabolized and then slowly washed out. Particular care must be taken when using this model for extrapolating *PPf* values at late times because it may yield negative values. In this case, a nonlinear constraint should be used dur-

ing the estimation of the parameters (i.e. constraining $yPPf(t_{end}) \geq 0$ with $t_{end}$ representing the time of the end of the scan).

### Exponential models

These models are characterized by a (multi)exponential decay. With minor variations, they have been used for [$^{11}$C]NNC 756 [25], [$^{11}$C]flumazenil [26] and [$^{11}$C]-(*R*)-PK11195 [27], among others. A general formulation is

$$yPPf(t) = A_0 + \sum_{i=1}^{n} A_i e^{-\lambda_i t}, \quad \text{with} \quad \sum_{i=0}^{n} A_i = 1 \tag{1.8}$$

All parameters $A_0, A_1, \lambda_1, \ldots, A_n, \lambda_n$ are $\geq 0$ where $n$ is an integer, usually $\leq 3$. In the variation used for [$^{11}$C]-(*R*)-PK11195 [28] the exponential decrease approached an oblique asymptote (Table 1.1). Similarly to the extended Hill model, nonlinear constraints may be necessary when using an oblique asymptote, because extrapolations at late times may yield negative values. Although these models are widely used in literature, they generally perform poorly during the initial phase of the *PPf*, because the *PPf* may decrease more slowly than what the exponential decay would predict [20].

### Modeling the arrival of radiometabolites

The aforementioned models can be extended to include a delay term, $t_0$, which represents the interval before radiometabolites appear in plasma [16] [29][26] [28]. The models $yPPf(t)$ are thus modified by substituting $t$ with $(t-t_0)$ and constrained to be equal to 1 for $t \leq t_0$.

Moreover, the models might start from an initial value ($PPf_0$) lower than 1. This is done to account for the presence of co-injected radiochemical impurities and the rapid formation of radiometabolites in the body during, for example, the first pass of the radioligand through the lungs [17]. This can be included in the model by multiplying $yPPf(t)$ by $PPf_0$ [30] or by subtracting $(1 - PPf_0)$ from $yPPf(t)$ [17]. The term $PPf_0$ can be estimated along with the model parameters or can be fixed to the value measured in the first sample, provided that the first sample is acquired early after injection. Oikonen [31] proposed to use the estimated $PPf_0$ to correct for the metabolism that intervenes during sample handling, i.e. the metabolism of the parent during the interval between blood drawing and analysis. It would be preferable, however, to chemically inhibit blood metabolism at the time of sample collection [32].

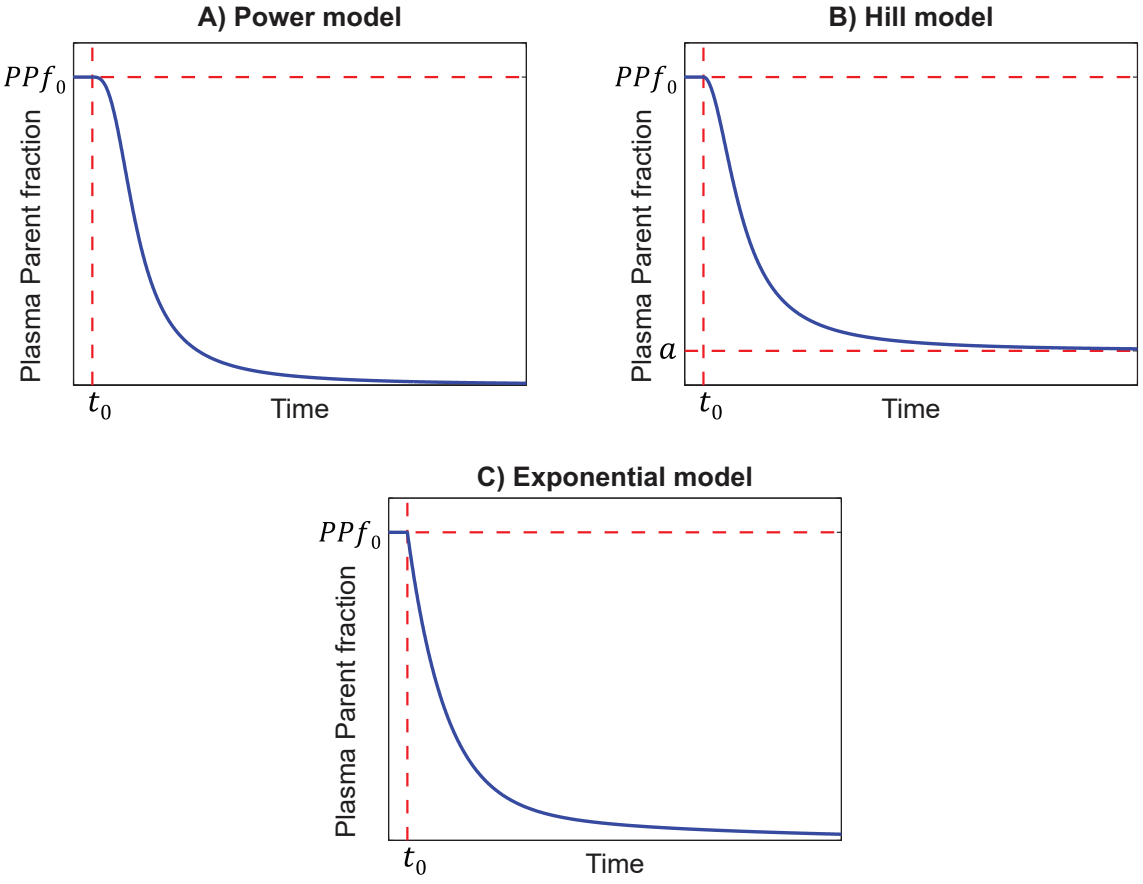


Figure 1.5: *Figure represents the power (A), Hill (B), and exponential (C) models for plasma parent fraction modeling. All models allow accounting for the metabolite delay ($t_0$) and non-unitary initial plasma parent fraction value ($PPf_0$). In addition, the Hill model allows accounting for the final plateau (a).*

### Compartmental models

*yPPf* models are empirical functions whose purpose is to describe plasma parent data, without necessarily taking into account the underlying physiological processes. Accounting for the physiology of the radioligand could nevertheless be possible by implementing compartmental models. Huang and colleagues [33] developed a generalized compartmental model to describe the conversion of an injected radiotracer into its radiometabolites. The model uses the total activity in plasma as input and the concentration of each radiometabolite as output. By identifying the model parameters, the full, noise-free time course of the parent concentration in plasma can be estimated. The main limitation of this approach is that the concentration of each radiometabolite in plasma must be measured. In general, HPLC analyses are optimized to separate the parent from the radiometabolites and not to isolate multiple different radiometabolites. Carson and colleagues [34] simplified this approach by lumping all the radiometabolites in a single compartment. Another variation included a compartment for the

red cells [35]. However, due to their complexity, compartmental models have been used only for few radioligands, i.e. [$^{18}$F]FDOPA [35] [36] [37], [$^{15}$O]O2 [33], [$^{11}$C]raclopride [34] and [$^{11}$C]Thymidine [38].

**Accounting for measurement errors**

When information on measurement error is available, parameters can be estimated by weighting each data point according to the inverse of its variance [3]. The measurement error of the *PPf* samples is assumed to be additive, uncorrelated, with zero mean and unknown variance. In most studies, the variance is assumed equal for all samples, which is equivalent to not weighting the data.

However, some studies assumed that the *PPf* variance is based on Poisson statistics of the area-under-the-curve of parent peaks ($AUC_p$) measured from radio-HPLC [39] [21], that is:

$$\mathrm{Var}(PPf) = AUC_p \tag{1.9}$$

This formula is based only on the statistic of the parent peak, while *PPf* is derived from both parent and radiometabolites peaks ($AUC_{met}$). Considering both contributes, the resulting formula is:

$$\mathrm{Var}(PPf) = \gamma \cdot \frac{AUC_p \cdot AUC_{met}}{(AuC_p + AUC_{met})^3} \tag{1.10}$$

where $\gamma$ is a proportional constant which is estimated *a posteriori*. The full derivation of this formula is presented in Appendix C.1.

Another formulation of *PPf* variance was derived by Wu and colleagues [14] for a HPLC equipped with a fraction collection system. The activity ($v_i$, where $i$ stands for the $i$-th fraction) and the associated standard deviation ($\sigma_i$) were measured with a well counter. The *PPf* variance was thus calculated as:

$$\mathrm{Var}(PPf) = \frac{(\sum_{i\notin I} V_i)(\sum_{i\in I} \sigma_i^2) - (\sum_{i\in I} V_i)(\sum_{i\notin I} \sigma_i^2)}{(\sum_i v_i)^2} \tag{1.11}$$

where $I$ is the set of indices of the fractions containing the parent.

Table 1.1: *Plasma Parent fraction models used in the literature*

| Tracer | Equation | References |
|---|---|---|
| **Power model** | | |

continued . . .

. . . continued

| Tracer | Equation | References |
|---|---|---|
| [$^{11}$C]MDL 100,907 | $\left[1+(at)^2\right]^{-b}$ | [15] |
| [$^{11}$C]MPDX | | [40] |
| [$^{18}$F]CPFPX | $\begin{cases} 1, & t \le t_0 \\ \left[1+(a(t-t_0))^b\right]^{-c}, & t \le t_0 \end{cases}$ | [16] |
| [$^{11}$C]MDL 100,907 | $\left[1+(at)^2\right]^{-b} - (1 - PPf_0)$ | [17] |
| **Hill model** | | |
| [$^{11}$C]WAY-100635 | $1 - \frac{at^b}{c+t^b}$ | [14] [18] |
| (*R*)-[$^{11}$C]verapamil | | [19] |
| [$^{11}$C]PE2I | | [41] |
| [$^{11}$C]flumazenil | | [20] |
| [$^{18}$F]FDDNP | | [42] |
| [$^{11}$C]DPA-713 | | [43] |
| [$^{11}$C](*R*)-PK11195 | | [44] [45] |
| [$^{11}$C]SD5024 | | [39] |
| [$^{11}$C]ORM-13070 | $1 - \frac{a\,(t-t_0)^b}{c+(t-t_0)^b}$ | [46] |
| [$^{18}$F]PBR111 | $\left[\left(1 - \frac{t^3}{t^3+10^a}\right)^b + c\right] \Big/ (1+c)$ | [47] |
| [$^{11}$C]PBR28 | | [48] |
| [$^{11}$C]carafentanil | $1 - \frac{at}{b+t}$ | [49] |
| [$^{11}$C]FLB | $1 - \frac{a+bt}{(c/t)^d+1}$ | [22] |
| [$^{11}$C]PiB | | [23] |
| [$^{18}$F]FLT | | [24] |
| [$^{68}$Ga]BAPEN | $\begin{cases} PPf_0, & t \le t_0 \\ PPF_0 + \frac{(a-PPf_0)\,(t-t_0)^b}{c+(t-t_0)^b}, & t \le t_0 \end{cases}$ | [50] |

continued . . .

. . . continued

| Tracer | Equation | References |
|---|---|---|
| **Exponential model** | | |
| L-[1-$^{11}$C]leucine | $\begin{cases} 1, & t \leq t_0 \\ Ae^{-\beta(t-t_0)} + 1 - A, & t \leq t_0 \end{cases}$ | [29] |
| [$^{11}$C]flumazenil | | [26] |
| [$^{11}$C]flumazenil | | [51] |
| [$^{11}$C]NNC 756 | | [25] |
| [$^{11}$C]DAA1106 | $Ae^{-\beta_1 t} + (1 - A)e^{-\beta_2 t}$ | [52] |
| [$^{11}$C]GB67 | | [53] |
| [$^{18}$F]DPA-714 | | [54] |
| [$^{11}$C](*R*)-PK11195 | $1 - A(2 - e^{-\beta_1 t} - e^{-\beta_2 t})$ | [27] |
| [$^{11}$C]L-deprenyl | | [55] |
| [1-$^{11}$C]Acetate | $Ae^{-\beta_1 t} + (1 - A)$ | [56] [57] |
| [$^{11}$C]DPN | | [58] |
| [$^{11}$C]-(+)-PHNO | | [59] |
| [$^{11}$C](*R*)-PK11195 | $(1 - A)e^{-\beta t} + A - Bt$ | [28] |
| **Others** | | |
| [$^{11}$C]raclopride | $1 - \frac{A(e^{-\beta_1 t} - e^{-\beta_2 t}) * C_{tot}(t)}{C_{tot}(t)}$ where $C_{tot}(t)$ is the total activity in plasma | [34] |
| [$^{11}$C]DASB | $t^a \left(A_1 e^{-\beta_1 t} + A_2 e^{-\beta_2 t}\right)$ | [13] |
| [$^{11}$C]GR103545 | $PPf_0 \left(1 - b\frac{\int_0^t e^{-u} u^{d-1} du}{\int_0^\infty e^{-u} u^{d-1} du}\right)$ | [30] |

## 1.4 Modeling the input function

In general, the time course of a PET input function can be organized in three parts: 1) a period of zero activity at the beginning of its time course due to the tracer delivery, 2) a rapid rising period, and 3) an exponential-like clearance phase.

One of the first general model to fit the arterial input function was proposed by Feng and colleagues in [60]. Feng's model was derived by the analytical solution of a blood circulation system compartmental modeling describing the radiotracer transportation through the human body. This model was validated for [$^{18}$F]FDG assuming a bolus injection of tracer. Feng's model formulation is:

$$yC_p(t) = \begin{cases} 0 & t < t_0 \\ A_1 (t - t_0) e^{-a_1(t-t_0)} + \sum_{i=2}^{3} A_i \left( e^{-a_i(t-t_0)} - e^{-a_1(t-t_0)} \right) & t \geq t_0 \end{cases} \tag{1.12}$$

with $t_0$ indicating the initial delivery phase.

In practice, the radiotracer injection is not instantaneous but lasts from some tens of seconds to few minutes. To describe this kind of behavior a second model was presented as variation of Feng's model and then extensively used in the literature. This consists in a straight line to the $C_p$ peak followed by a tri-exponential decay. The formulation of the tri-exponential model is given by:

$$yC_p(t) = \begin{cases} 0 & t < t_0 \\ \frac{\sum_{i=1}^{3} A_i}{t_{peak} - t_0} (t - t_0) & t_0 \leq t < t_{peak} \\ \sum_{i=1}^{3} A_i e^{-a_i(t-t_{peak})} & t \geq t_0 \end{cases} \tag{1.13}$$

with $t_{peak}$ indicating the input function peak time. However, while fairly describing the decreasing phase of the input function, the tri-exponential model provides only a crude representation of its rising phase.

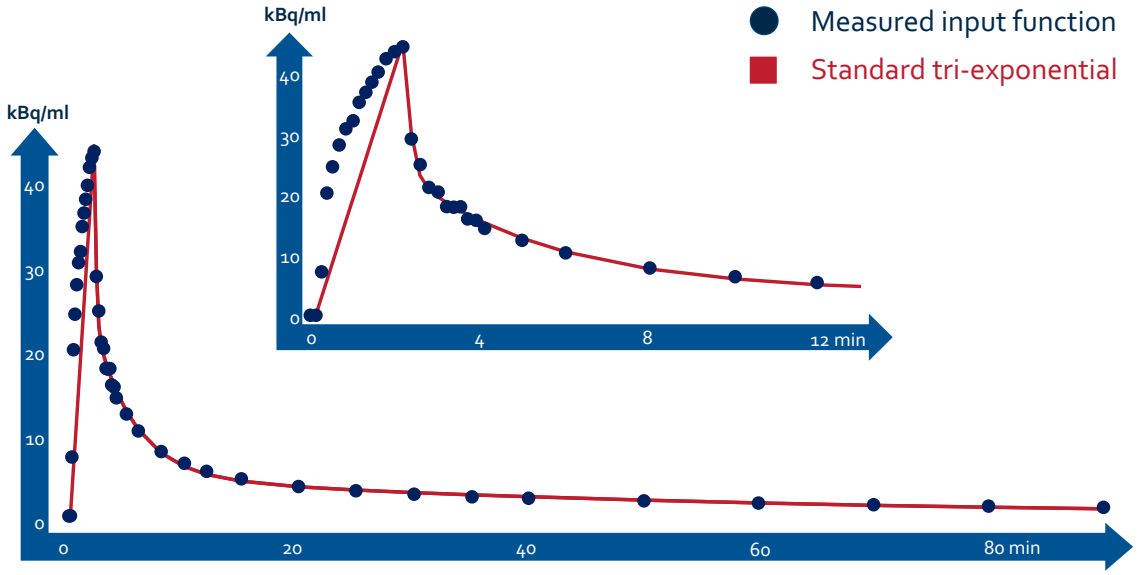


Figure 1.6: *Figure represents the fit (red line) obtained with the standard tri-exponential model of the measured input function (blue points) in a representative L-[1-$^{11}$C]leucine subject. The injection protocol consisted of a short tracer infusion with duration equal to 2 minutes. When the duration of the injection is* $\geq$ *1 min, the standard tri-exponential model provides a bad description of the rising phase, as can be observed in the zoomed panel.*

Chapter 2

# Improved Models for Plasma Parent Fraction

In the literature several different *yPPf* models are used, as shown in section 1.3. Although these are defined by different formulas, they all are empirical functions chosen with the unique purpose of describing the *PPf* data. Thus, they are commonly applied without explicitly considering underlying physiologic processes of radioligand metabolism (e.g., the rate of metabolism) or experiment variables (e.g., radioligand injection time). Some attempts to account for the physiology of radioligand metabolism have been conducted with compartmental models (see section 1.3). However, these methods require *a priori* knowledge of the biochemical pathways of the radioligand, which are radioligand specific and most of times not completely known.

In this chapter, a new modeling approach is presented, which could help improving the description of the *PPf* measures by taking into account the duration of the radioligand injection. This method lies in between the full physiologic modeling of the metabolism kinetic and the experiment-unrelated analytical function. In fact, on the one hand, it allows including an experiment-specific variable into account while on the other hand it does not lose generality since it can be applied to any of the aforementioned analytical functions that are currently the mostly used *PPf* models. This method was validated on three radioligands ([$^{11}$C](*R*)-rolipram, [$^{11}$C]NOP-1A, and [$^{11}$C]MePPEP), which exhibit different blood and radiometabolite kinetics and for which an unusually high number of *PPf* samples was available (on average 15 per subject).

## 2.1 Materials and methods

When the radioligand is administrated as a bolus, the injection duration is assumed to be instantaneous, even if in practice it can last from some tens of seconds up to few minutes. This may affect the initial phase of the *PPf* curve since the organism is already metabolizing a part of the radioligand while the rest has just been injected. Thus, in the first blood samples a mixture of newly injected and recirculating radioligand might be present. To account for this effect, the injection was explicitly modeled as a boxcar function:

$$u(t,T) = \begin{cases} 0 & t < 0 \vee t > T \\ \frac{1}{T} & 0 \leq t < T \end{cases} \tag{2.1}$$

where $T$ represent the length of radioligand injection. $u(t,T)$ is assumed to be the input of a dynamic system whose impulse response function is a mathematical function such as the ones currently used to model the *PPf*. The final formulation, which was called the convoluted model, is given by:

$$yPPf^{C}(t) = \frac{yPPf * u(t,T)}{\int_0^t u(s,T)\mathrm{d}s} \tag{2.2}$$

where $yPPf^{C}(t)$ is the convoluted version of the radioligand-specific model $yPPf$ and $*$ is the convolution operator. The integral at the denominator ensure the normalization of the model in the interval $[0;1]$. Notably, the amplitude of the boxcar function appears at both the numerator and the denominator and can therefore be ignored. To note that this new mathematical description does not introduce any new parameter to be estimated because the value of $T$ is known from the experiment protocol.

### 2.1.1 Dataset

To test the validity of the convoluted $yPPf^{C}$ models compared with the standard ones, three different datasets acquired at the Molecular Imaging Branch of the National Institute of Mental Health (USA) were considered. The radioligands, characterized by different pharmacokinetic proprieties (i.e., faster or slower kinetics) were [$^{11}$C]NOP-1A, a nociceptin/orphanin FQ peptide receptor ligand ($N = 22$; $716 \pm 83$ MBq, scan duration = 120 minutes) [61]; [$^{11}$C]MePPEP, an inverse agonist for cannabinoid receptor type 1 receptors ($N = 20$, $657 \pm 76$ MBq, scan duration = 90 minutes) [62]; and [$^{11}$C]($R$)-rolipram, a ligand for phosphodiesterase 4 (an enzyme that metabolizes cyclic adenosine monophosphatase) in the brain ($N = 24$,

420 ± 144 MBq, scan duration = 90 minutes) [63]. Recruitment processes and eligibility criteria are described in the original publications. The protocol was approved by the Ethics Committee of the National Institutes of Health; all subjects gave written informed consent. All the studies were conducted according to the Declaration of Helsinki. Radioligands were injected intravenously over 1 minute using an automated pump, and blood samples were manually drawn from the radial artery at 15-second intervals until 120 or 150 seconds, and then at increasingly longer intervals until the end of the scan. Each input function consisted of about 22 individual samples.

#### Blood sample processing

Plasma was first separated from blood cells by centrifugation. Activity in both the whole blood $C_b$ and total plasma $C_{tot}$ were measured on each sample. Sample counts were consistently monitored and variable volumes were aliquoted to keep the counting error in each sample $< 2.5\%$ ( 2000 counts) at 1 s.d. Radiometabolite separation from parent plasma concentration was performed by HPLC on almost every blood sample, as described in [9] obtaining an unusually high number of *PPf* samples per subject (17 ± 2 for [$^{11}$C]NOP-1A; 13 ± 2 for [$^{11}$C]MePPEP, and 13 ± 1 for [$^{11}$C](*R*)-rolipram).

### 2.1.2 Radiometabolite Data Modeling and Statistical Analysis

#### Model parameter quantification

All three *yPPf* standard models (power, Hill, and exponential) and their corresponding convoluted versions were fitted to the *PPf* measures of each subject. All models were considered in their more general form, i.e. including a delay term $t_0$ and an initial value $PPf_0$ different from 1. The parameters for each model and each subject were estimated using a maximum-likelihood nonlinear estimator with a relative weighting scheme based on HPLC measurements. Measurement error was assumed to be additive and uncorrelated with zero mean and variance calculated with equation 1.10. Weights were then chosen as the inverse of the variance, and the proportionality constant $\gamma$ was estimated *a posteriori* as in [64].

#### Criteria for model comparison.

The performance of the standard versus the convoluted version for power, Hill, and exponential model classes were compared. Then, for each radioligand, the optimal model to describe the *PPf* measures was selected considering the following performance indices:

1. Weighted residual sum of squares (WRSS): the Akaike's Information Criterion [65], which balances the WRSS with the number of model parameters, is generally used to compare different models. However, because all the models considered had the same number of parameters, WRSS was used to investigate model performance instead of Akaike's Information Criterion. In particular, we considered the percentage difference between the WRSS of convoluted and standard models, calculated as: $\%diff = (WRSS_{standard} - WRSS_{convoluted})/WRSS_{standard}$.

2. Coefficient of variation (CV) of the model parameter estimates: this index returns information about estimate precision. It was calculated for each model and each subject from the standard deviation derived by the inverse of the Fisher information matrix, and expressed as a percentage of the estimated parameters. To note that, even if the *yPPf* model parameters do not have any physiologic meaning about metabolite metabolism, the associated CVs are important since they return an indirect measure of the model robustness.

3. Percentage of outliers, defined as the fraction of subjects in which at least one estimated parameter had a $CV > 1000\%$, excluding $t_0$. Outliers are not considered in the calculation of the other performance indices as they would bias their estimates. Nevertheless, the percentage of outliers is indicative of the model robustness.

4. Residual zero-line crossing: this index represents an indirect measure of the polarization of the residuals. It is calculated as the number of times that the weighted residuals cross the zero line, normalized by $n - 1$, where $n$ is the total number of samples. The expected value for the zero-line crossing is 0.5 (as from a Bernoulli distribution with $P = 0.5$ and $n - 1$ trials). The lower this number, the more polarized the residuals.

**Impact on tissue kinetic quantification**

The optimal *yPPf* model selected in the previous step (both in its standard and convoluted version) was used to perform radiometabolite correction. Thus, two input functions were generated for each subject:

$$yC_p^S(t) = C_{tot}(t) \cdot yPPf(t) \tag{2.3}$$

$$yC_p^C(t) = C_{tot}(t) \cdot yPPf^C(t) \tag{2.4}$$

For the three radioligands considered, the optimal model to describe the kinetic behavior at regional level was a two-tissue compartmental model (2TCM)[61] [62] [63]. The rate constants $K_1\left(\frac{mL}{cm^3}/min\right)$, $k_2\,(1/min)$, $k_3\,(1/min)$, $k_4\,(1/min)$, and $V_b\,(unitless)$ were estimated for each region with a maximum-likelihood nonlinear estimator. The parameters of interest were:

- $V_T = \frac{K_1}{k_2}\left(1 + \frac{k_3}{k_4}\right)$: the total volume of distribution ($mL/cm^3$), which equals the ratio at equilibrium of the concentration of radioligand in the brain to that in the plasma [66];
- $BP_P = \frac{K_1 k_3}{k_2 K_4}$: the binding potential ($mL/cm^3$), which refers to the ratio at equilibrium of specifically bound radioligand to that in the plasma [66].
- $BP_{ND} = \frac{k_3}{k_4}$: the nondisplaceable binding potential (*unitless*), which refers to the ratio at equilibrium of specifically bound radioligand to that of nondisplaceable radioligand in the tissue [66].

Positron emission tomography data measurement error was assumed to be additive and uncorrelated, with zero-mean and Gaussian distribution. We defined the diagonal elements of the error covariance matrix according to the formula originally proposed by Mazoyer and colleagues [67]:

$$\mathrm{Var}\,(C_i) = \gamma \frac{C_i}{\Delta_{t_i}} \tag{2.5}$$

where $C_i$ represents the activity of the radioligand in a specific volume of interest at the frame $i$, and $\Delta_{t_i}$ is the duration of frame $i$. The proportionality constant $\gamma$ is, as for the radiometabolite fit, an unknown scale factor estimated *a posteriori* as in [64].

All the data were corrected for the radioligand decay and blood arterial delay (defined as the time difference between the blood arrival from the radial artery and the brain) [68]. The correlation between the $V_T$ values obtained with the two different inputs, i.e., $yC_p^S$ and $yC_p^C$, was calculated with Pearson's $R^2$ coefficient for all the regions for each subject.

The mean relative difference (MRD) was calculated as the average of the absolute value of the relative differences, i.e. $RD = 2 \cdot \left(V_T^S - V_T^C\right)/\left(V_T^S + V_T^C\right)$. The same indices were considered also for $BP_P$,$BP_{ND}$, and the microparameters (i.e., $K_1$, $k_2$, $k_3$,and $k_4$) to evaluate which ones are the most influenced by the different radiometabolite correction.

## 2.2 Results

### 2.2.1 Convoluted versus standard models

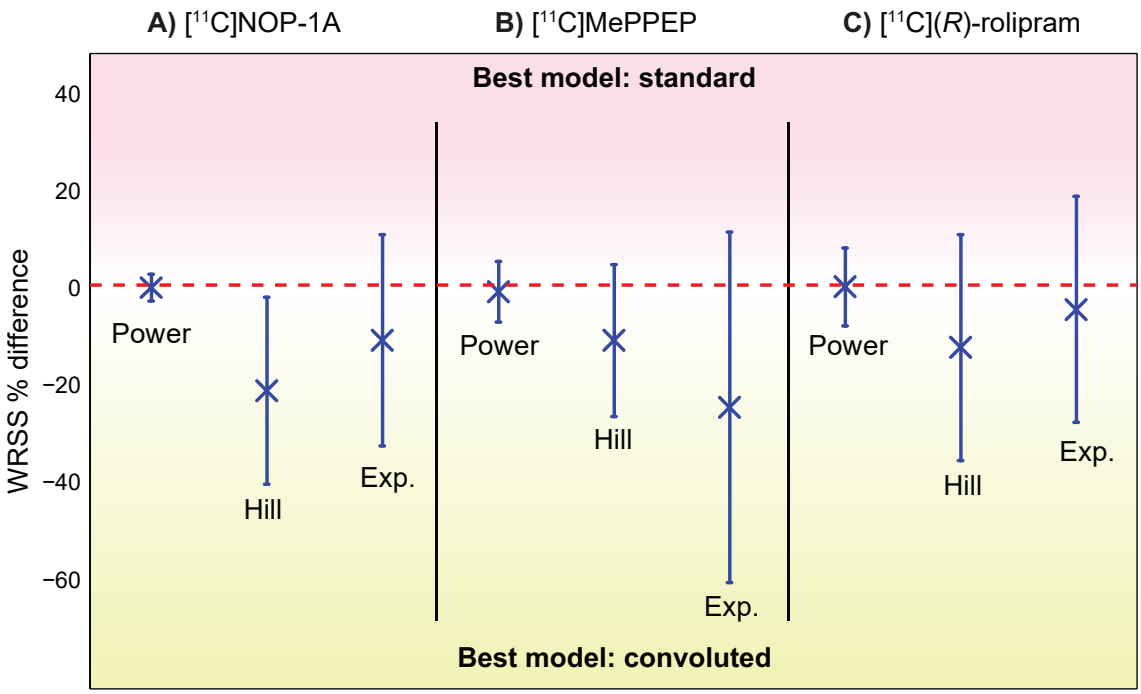


Figure 2.1: ***The effects of radioligand injection on plasma parent fraction modeling.*** *The figure reports the weighted residual sum of square (WRSS) percentage difference, computed between convoluted plasma parent fraction $yPPf^C$ modeling (accounting for the radioligand injection time) and standard yPPf modeling (applied without any information about radioligand injection time).* ***A***, ***B***, *and* ***C*** *refer to [$^{11}$C]NOP-1A, [$^{11}$C]MePPEP, and [$^{11}$C](R)-rolipram analysis, respectively. For each radioligand, all the yPPf models were tested and intersubject mean (x) and variability (error bars) of percentage difference between convoluted and standard yPPf modeling are reported. Values falling in the red band (top) means the WRSS of the standard model is lower than the corresponding WRSS of the convoluted model (i.e., standard model performs better than convoluted one). The opposite for the yellow band (bottom).*

The use of a convolution term to account for the duration of radioligand injection improved model fit performance for all radioligands and all *yPPf* models (Figures 2.1). In particular, the WRSS obtained using convoluted $yPPf^C$ models was always lower than the one obtained using the standard versions. However, the magnitude of the relative WRSS difference depended on the *yPPf* function; it was relatively small with the power model (1% ± 6% on average), but significantly greater with Hill and exponential (up to 21% and 25%, respectively). Since convoluted models

better described *PPf* data than standard models, the optimal model selection for each radioligand is presented using only the former.

### 2.2.2 Selection of the optimal plasma parent fraction model

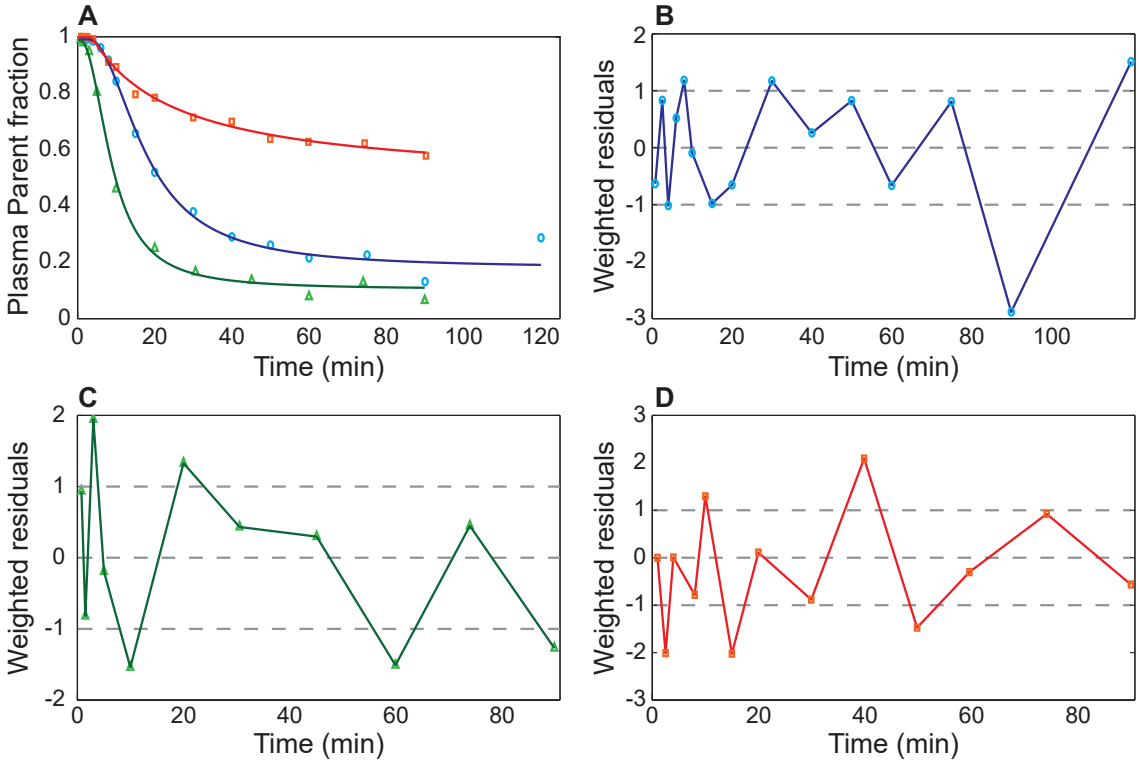


Figure 2.2: ***Optimal plasma parent fraction modeling in [$^{11}$C]NOP-1A, [$^{11}$C]MePPEP, and [$^{11}$C](R)-rolipram positron emission tomography (PET) data.*** *(**A**) Shows an example of the optimal plasma parent fraction (yPPf) model in three representative subjects belonging to the three analyzed PET datasets; blue open circles, green triangles, and red squares indicate [$^{11}$C]NOP-1A, [$^{11}$C]MePPEP, and [$^{11}$C](R)-rolipram metabolite data, respectively. (**B**-**D**) show the weighted residual time-activity course (PPf data - yPPf model prediction) for the same representative subjects (with the same order of datasets). Dashed lines indicated the $-1/+1$ confidence region as well as the zero line.*

Table 2.1: *PPf model selection*

| | | $a$ | $b$ | $CV$ $c$ | $PPf_0$ | $t_0$ | Outliers | zero-line crossing | WRSS |
|---|---|---|---|---|---|---|---|---|---|
| [$^{11}$C]NOP-1A | Power | 61% ± 51% | 199% ± 206% | 191% ± 193% | 0.3% ± 0.1% | 242% ± 132% | 5% | 0.37 | $2.24E^{-04} \pm 2.16E^{-04}$ |
| | Hill | 10% ± 80% | 13% ± 6% | 82% ± 42% | 0.2% ± 0.1% | 34% ± 22% | 5% | 0.48 | $1.00E^{-04} \pm 9.81E^{-05}$ |
| | Exp. | 12% ± 10% | 20% ± 12% | 170% ± 155% | 0.2% ± 0.1% | 6% ± 3% | 24% | 0.46 | $2.19E^{-04} \pm 1.95E^{-04}$ |
| [$^{11}$C]MePPEP | Power | 38% ± 35% | 140% ± 127% | 129% ± 116% | 0.2% ± 0.1% | 336% ± 299% | 0% | 0.46 | $3.03E^{-05} \pm 2.66E^{-05}$ |
| | Hill | 14% ± 80% | 10% ± 5% | 52% ± 40% | 0.1% ± 0.1% | 53% ± 149% | 0% | 0.60 | $1.77E^{-05} \pm 1.27E^{-05}$ |
| | Exp. | 70% ± 50% | 24% ± 26% | 89% ± 60% | 0.2% ± 0.1% | 14% ± 18% | 15% | 0.61 | $5.44E^{-05} \pm 5.62E^{-05}$ |
| [$^{11}$C](*R*)-rolipram | Power | 96% ± 122% | 79% ± 152% | 123% ± 149% | | 48% ± 67% | 17% | 0.56 | $1.11E^{-05} \pm 4.31E^{-05}$ |
| | Hill | 22% ± 20% | 13% ± 7% | 22% ± 12% | | 8% ± 6% | 0% | 0.54 | $1.38E^{-05} \pm 4.41E^{-05}$ |
| | Exp. | 15% ± 10% | 26% ± 20% | 21% ± 22% | | 5% ± 3% | 22% | 0.51 | $3.29E^{-06} \pm 5.48E^{-06}$ |

- CV: Coefficient of Variation of the parameter estimates (mean ± SD); reflects estimate reliability.
- Outliers: the percentage of subjects over the total who reported at least one parameter with a corresponding $CV > 1000\%$ (excluding $t_0$).
- Zero-line crossing: number of times that weighted residuals cross the zero line over the total number of residuals. The value reported is the mean between subjects, (excluding outliers).
- WRSS: Weighted Residuals Sum of Squares (mean ± SD)

For all radioligands, Hill convoluted was the optimal model (Table 2.1).

For [$^{11}$C]NOP-1A, the Hill model had the lowest mean WRSS ($1.00E-04 \pm 9.81E-05$), the lowest CVs for all parameters (excluding $t_0$), and the most random residuals (0.48 of zero-line crossing) among the three models (Table 2.1). In terms of outliers, parameter identification failed for only one subject. The good performances of the Hill model for [$^{11}$C]NOP-1A were visually corroborated by the good fit of the model to the *PPf* data (Figure 2.2A). The weighted residual time course was consistent with the assumption made for the error variance law (Figure 2.2B).

For [$^{11}$C]MePPEP, Hill convoluted had the lowest WRSS ($1.77E-05 \pm 1.27E-05$), the lowest parameter CVs ($t_0$ excluded) and random residuals (0.61 of zero-line crossing; Table 2.1). Notably, the exponential model did not achieve reliable parameter estimates in 15% of subjects. Visually, the Hill model well fitted the measured data (Figure 2.2A), and the weighted residuals (Figure 2.2C) were random, with zero mean and variance equal to one (in agreement with the assumption made for the variance error law).

When applied to the [$^{11}$C](*R*)-rolipram dataset, the *yPPf* models were simplified with $PPf_0$ constrained to 1. In fact, [$^{11}$C](*R*)-rolipram was obtained in high radiochemical purity (99.9% ± 0.2%) and impurities were thus negligible. The exponential model showed the lowest WRSS ($3.29E-06 \pm 5.48E-06$), but a substantial percentage of subjects (22%) had non-reliable parameter estimates (Table 2.1). In terms of parameter CV, both Hill and exponential models had similar precisions (ranging from 8% to 22% for Hill and from 5% to 26% for the exponential model), while the power model showed higher variability. Randomness of the residuals was comparable between the three models. However, Hill model did not yield any outliers, making it the preferred method to fit [$^{11}$C](*R*)-rolipram data. Figures 2.2A and 2.2D, show an example of a Hill model description of [$^{11}$C](*R*)-rolipram *PPf* and the weighted residual time course.

### 2.2.3 Impact on tissue kinetic quantification

The estimates of the macroparameters were comparable with the ones reported in the literature [61] [62] [63] [69] ([$^{11}$C]NOP-1A: $V_T = 8.90 \pm 1.53 mL/cm^3$, $BP_P = 2.69 \pm 0.94 mL/cm^3$, $BP_{ND} = 0.49 \pm 0.23$; [$^{11}$C]MePPEP: $V_T = 15.26 \pm 6.97 mL/cm^3$, $BP_P = 14.50 \pm 6.99 mL/cm^3$, $BP_{ND} = 24.86 \pm 11.07$; [$^{11}$C](*R*)-rolipram: $V_T = 0.59 \pm 0.12 mL/cm^3$, $BP_P = 0.30 \pm 0.08 mL/cm^3$, $BP_{ND} = 1.02 \pm 0.23$).

Among the three radioligands considered, [$^{11}$C]NOP-1A (Figure 2.3A) showed the greatest differences of the micro-parameters $k_3$ and $k_4$ (MRD = 18% ± 12% and 18% ± 14% respectively) obtained with the two input functions, yet the differences on the $V_T$ estimates were limited (MRD = 2% ± 2%). Correlation coefficient on $V_T$ was $R^2$ = 0.98 ± 0.04, range [0.86; 1]. Both measures of the binding potential, $BP_P$ and $BP_{ND}$, exhibited a greater difference (MRD = 8% ± 7% and MRD = 10% ± 8% respectively) and a lower correlation ($R^2$ = 0.88 ± 0.12 and $R^2$ = 0.90 ± 0.12 respectively) than $V_T$. Interestingly, $k_3$ and $k_4$ estimates were highly correlated (on average $R^2$ = 0.98 ± 0.03 and $R^2$ = 0.97 ± 0.07 respectively) but they showed a different range of correlation values ($k_3$: [0.90; 1], $k_4$: [0.69; 1]).

As regard [$^{11}$C]MePPEP (Figure 2.3B), negligible differences in both macro- and micro-parameter estimates (on average MRD < 3% and $R^2$ > 0.99) were observed.

Also [$^{11}$C](*R*)-rolipram (Figure 2.3C) presented negligible differences on the macro-parameters (MRD = 1% ± 1% and $R^2$ = 0.99 ± 0.02 for $V_T$, MRD = 3% ± 2% and $R^2$ = 0.98 ± 0.06 for $BP_P$, MRD = 5% ± 2% and $R^2$ = 0.97 ± 0.11 for $BP_{ND}$). Nevertheless, there was an important impact on the modeling of the *PPf* on the micro-parameters on 4 subjects out of 24. In particular, $k_3$ and $k_4$ showed the highest MRD and the smallest correlation (MRD up to 46% and $R^2$ down to 0.70 for $k_3$).

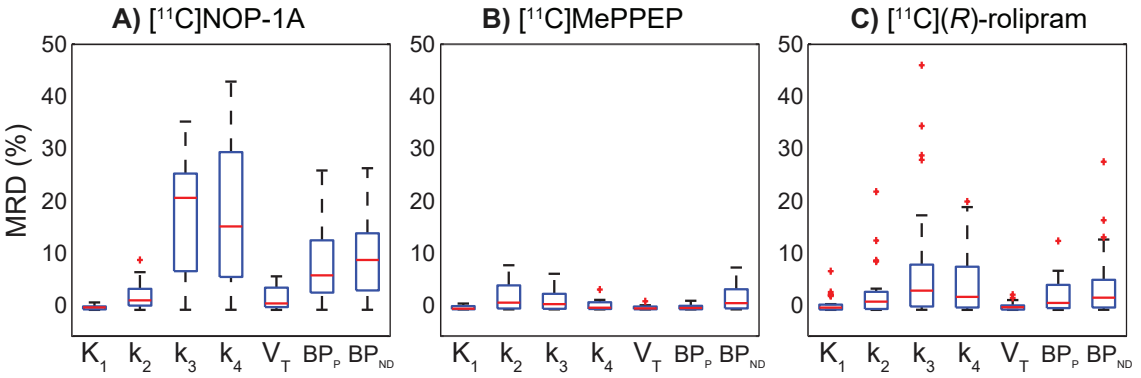


Figure 2.3: ***Distributions of mean relative differences (MRDs) for micro- and macroparameters estimated with*** $yC_p^S$ ***and*** $yC_p^C$***.*** *Figure shows the boxplots of the MRDs between* $K_1$, $k_2$, $k_3$, $k_4$ *and* $V_T$,$BP_P$,$BP_{ND}$ *estimated using the input function corrected with the standard plasma parent fraction (yPPf) model and the input function corrected with the convoluted* $yPPf^C$ *model. The MRD was calculated between all the regions for each subject.* ***A***, ***B***, *and* ***C*** *show the results for [*$^{11}$*C]NOP-1A, [*$^{11}$*C]MePPEP, and [*$^{11}$*C](R)-rolipram, respectively.*

## 2.3 Discussion

This work sought to improve the accuracy of the estimation of the input function through a better modeling of the plasma parent fraction for the radiometabolite correction. The aim was reached by introducing a modification of the existing *yPPf* models, which improved the description of the *PPf* measures by taking into account the duration of the radioligand injection. Three different radioligands with different blood kinetics and with a rich sample size were used to validate our modeling approach.

In this chapter, the standard *yPPf* models available in the literature were used to obtain a better description of the *PPf* measured data by incorporating the duration of radioligand injection into their mathematical formula (thereby creating convoluted models). These convoluted models always performed better than standard models without increasing their complexity in terms of the number of parameters to be estimated. In particular, the convoluted versions of both the Hill and exponential models improved the *PPf* measure description up to 21% and 25% in terms of mean WRSS. All radioligands were injected over the course of 1 minute. It is expected that the longer the injection time, the higher the impact.

The Hill convoluted model was selected as the optimal model for the three datasets in this study ([$^{11}$C]NOP-1A, [$^{11}$C]MePPEP, and [$^{11}$C](*R*)-rolipram). This model provided accurate and precise parameter estimates, and was flexible enough to describe the final plateau in all the analyzed *PPf* data. As the present study confirmed, the Hill function works well across different radioligands. However, it may not be suitable for some radioligands that display very particular shapes of the input function. For instance, the plasma parent concentration of [$^{11}$C]DASB [13] actually increases over time, most likely because of an initial trapping of the parent in the lungs; this would not be amenable to modeling with Hill function.

In terms of impact on tissue estimates, the convoluted $yPPf^C$ models showed negligible influence on the macroparameter $V_T$ and varying impact on $BP_P$,$BP_{ND}$, and the microparameters, which can be more sensitive to the shape of the input function (e.g., 18% of MRD of $k_3$ and $k_4$ in [$^{11}$C]NOP-1A). However, it must be taken into account that the true input function is not known but, as assumed in other previous works [14] [70], a better description of the *PPf* should lead to a more correct quantification of the tissue parameters. No clear relationship was found between total plasma or *PPf* kinetics and the impact of modeling on the final tissue estimates. Among the three datasets, [$^{11}$C]MePPEP had the fastest kinetics,

while [$^{11}$C](*R*)-rolipram showed the slowest ones. Nevertheless, [$^{11}$C]NOP-1A had the highest sensitivity to *yPPf* and modeling. No relationship was found between the MRD of the tissue estimates and the estimates themselves either.

This work used an unusually rich dataset acquired at the Molecular Imaging Branch, National Institute of Mental Health, USA. The high number of HPLC measurements (almost one per blood sample) provided optimal conditions for selecting the best *yPPf* models and allowed us to avoid the use of complex modeling approaches, particularly nonlinear mixed effects ones [70]. This data-rich environment was exploited not only to derive the optimal model for describing radiometabolite time course, but also to define a consistent and theoretically justifiable error model for the definition of *wPPf* modeling weights. The error law used here accounted for the fact that the *PPf* is the ratio of two measurements obtained from HPLC, and both of them are affected by a measurement error. These two independent errors contribute to the final *PPf* error according to the principle of propagation of uncertainty (see Appendix C.1). This error model was validated *a posteriori* by analyzing the weighted residual randomness, its mean value (expected to be zero), and variance (expected to be 1). Other error laws (for instance, based on the unitary variance of the weighted residuals) failed to satisfy the hypothesis (data not shown). Notably, the residual polarization was checked using the zero-line crossing values while normality was tested using the Anderson-Darling test. We tested three other error laws: the first assumed the variance of the error to be constant among the *PPf* data, the second assumed it proportional to the *PPf* data, and the third was the Poisson error law. The weighted residual analysis showed that all of them overestimated the variance of the first samples and underestimated the variance of the lasts.

## 2.4 Conclusion

Including the injection duration in the *yPPf* model description allows convoluted models to better describe the data compared with standard models. For the radioligands studied, the Hill convoluted model provided better fits and more precise parameter estimates than exponential fitting and power models. The final kinetic results were influenced by how the input function was generated, although the magnitude of this effect depended on the radioligand and on the parameters considered.

# Chapter 3

# Physiological Model For The Input Function

After correcting for radiometabolites, the resulting input function consists of noisy and discrete samples. Consequently, a model-based description of the arterial samples is preferred. The most common models proposed in literature are the Feng's model (Equation 1.12) [60] and the standard tri-exponential model (Equation 1.13) [71], but they both present some limitations: Feng's model was developed for instantaneous bolus injection while in practice the injection lasts from some tens of seconds to few minutes; tri-exponential model employs a straight line from the starting time to the peak followed by a tri-exponential decay but it provides a poor description of the initial part of the curve [72].

In the previous chapter a method which included the information of the tracer injection length in the modeling of the radiometabolite fraction was proposed and validated. The injection of tracer was modeled as a boxcar function and applied as an input of an empirical dynamic system through the convolution operator. Here, this approach is extended also to the input function modeling. However, differently from the *yPPf* model, the form of the dynamic system is derived from the theory of tracer-tracee, resulting in a more physiological model. Two novel $yC_p$ models (named "convoluted models"), based on two different dynamic systems, are hence proposed in order to ameliorate those currently used in literature ("standard models") and to derive a physiological description of the $C_p$ to be used in the subsequent PET quantification step. Eight different PET datasets, acquired multi-center, are considered for the $yC_p$ model evaluation, for a total of 201 PET exams.

## 3.1 Materials and methods

### 3.1.1 Tracer-tracee theory and the input function model

The tracer-tracee theory for biological systems states that the tracer kinetics can be described with a linear and time-invariant (LTI) model independently from the fact that the tracee system is linear or not [3]. The general solution of a LTI system is a sum of exponential functions, with the exponents ($a_i$) being the system eigenvalues and $A_i$ their coefficients:

$$h_p(t) = \sum_{i=1}^{N} A_i e^{-a_i t} \tag{3.1}$$

Equation 3.1 represents the impulse response function (IRF), that is the output of a system following an impulse input. The same theory can be applied to a PET experiment to describe the tracer kinetics in blood, with the output being the plasma tracer concentration, and the input corresponding to the injection of the tracer. In research PET setting, bolus injection is common practice, but the tracer administration is not instantaneous and may last from 20-30 seconds up to 1-2 minutes. This was modeled with the same boxcar function $u(t)$ defined by equation 2.1 for radiometabolites. The final model for the parent plasma activity is therefore given by the convolution between the tracer injection $u(t)$ and the system impulse response function $h_p(t)$:

$$yC_p(t) = \begin{cases} 0 & t \leq t_0 \\ h_p(t - t_0) * u(t) & t > t_0 \end{cases} \tag{3.2}$$

where $t_0$ models the tracer arrival time from the injection at measurement site. To note that the delay term is included in the IRF and not in $u(t)$ as it depends on the underlying system and it is independent from the input [60].

In [60] it was suggested that the tracer behavior in the circulatory system may have a pair of repeated eigenvalues, i.e. the solutions to the characteristic equation associated with the LTI system contain a double root. In this case, the system impulse response would have the following form:

$$h_p(t) = A_0 t e^{-a_1 t} + \sum_{i=1}^{N} A_i e^{-a_i t} \tag{3.3}$$

where $-a_1$ is the repeated eigenvalue. To note, assuming an impulse as input, this would result in the Feng's model of equation 1.12

In total two new convoluted models were introduced: the tri-exponential convoluted model, which used equation 3.1 with $N = 3$ as system impulse response, and the Feng convoluted model, which instead used equation 3.2 as system impulse response, again with $N = 3$. These two models were compared versus the standard models, i.e. Feng's model (equation 1.12) and the tri-exponential standard model (equation 1.13).

### 3.1.2 Dataset

Eight datasets acquired in four different PET centers were used to compare convoluted versus standard models:

- [$^{11}$C]MePPEP, an inverse agonist for cannabinoid receptor type 1 receptors ($N = 20$, 657 ± 76 MBq, scan duration = 90 minutes) acquired at the Molecular Imaging Branch (MIB) of the National Institute of mental Health (NIH) (USA) [62];
- [$^{11}$C]NOP-1A, a nociceptin/orphanin FQ peptide receptor ligand ($N = 22$; 716 ± 83 MBq, scan duration = 120 minutes) acquired at the NIH-MIB [61];
- [$^{11}$C](*R*)-rolipram, a ligand for phosphodiesterase 4 (an enzyme that metabolizes cyclic adenosine monophosphatase) in the brain ($N = 24$, 420 ± 144 MBq, scan duration = 90 minutes) acquired at the NIH-MIB [63];
- [$^{11}$C]PBR28 binds to the translocator protein, a marker of brain immune activation ($N = 23$, 680 ± 14 MBq, scan duration = 90 minutes) acquired at the NIH-MIB [73]
- L-[1-$^{11}$C]leucine is one of the 20 standard amino acids and it has a relevant role in the constitution and maintenance of the muscular tissue ($N = 49$, 925 ± 187 MBq, scan duration = 90 minutes) acquired at the Section on Neuroadaptation and Protein Metabolism (SNPM) of NIH [74]
- [$^{18}$F]FDG, a glucose analog widely employed for studying tissue metabolism ($N = 15$, 180 ± 12 MBq, scan duration = 90 minutes) acquired at the PET Research Center, University of Pittsburgh [75]
- [$^{11}$C]PiB stands for Pittsburgh Compound-B, an analog of thioflavin T, radiotracer used in PET scans to image beta-amyloid plaques in neuronal tissue

($N$ = 18, 560 ± 160 MBq, scan duration = 90 minutes) acquired at the PET Research Center, University of Pittsburgh [75]

- [$^{11}$C]DASB is a compound that binds with high affinity and selectivity to the serotonin (5-hydroxytryptamine, or 5-HT) transporter ($N$ = 30, 570 ± 104 MBq, scan duration = 90 minutes) acquired at the Department of Radiology, Columbia University [13].

Table 3.1: *Dataset*

| Tracer | Number of subjects | Number of samples | Injection time (s) | PET Center |
|---|---|---|---|---|
| [$^{11}$C]MePPEP | 20 | 19 | 60 | NIH-MIB |
| [$^{11}$C]NOP-1A | 22 | 24 | 60 | NIH-MIB |
| [$^{11}$C]($R$)-rolipram | 24 | 23 | 60 | NIH-MIB |
| [$^{11}$C]PBR28 | 23 | 24 | 60 | NIH-MIB |
| L-[1-$^{11}$C]leucine | 49 | 41 | 120 | NIH-SNPM |
| [$^{18}$F]FDG | 15 | 38 | 20 | Univ. of Pittsburgh |
| [$^{11}$C]PiB | 18 | 30 | 20 | Univ. of Pittsburgh |
| [$^{11}$C]DASB | 30 | 31 | 30 | Columbia Univ. |

### 3.1.3 Parameter estimation and statistical analysis

The model for the measured input function $C_p$ is assumed as:

$$C_p = yC_p(\partial, t_i) + e(t_i) \tag{3.4}$$

where $t_i$ is the time of the i-th measurement, $yC_p(\partial, t_i)$ is one of the tested input function model with parameter vector $\partial$, and $e(t_i)$ is additive Gaussian noise with zero mean and variance equal to $\gamma B$:

$$e \sim N(0, \gamma B) \tag{3.5}$$

In this formulation $\gamma$ is an unknown constant and $B$ is a diagonal matrix (noise is assumed independent) whose elements are calculated as $1/z$ as commonly done with radiation measurements [76]. The parameters were hence estimated using a maximum-likelihood non-linear estimator with weights chosen as the inverse of the sample error variance. The unknown constant $\gamma$ was estimated *a posteriori* as in [64].

Model performances were compared using:

- Akaike Information Criterion (AIC) [65]: a paired t-test on the AIC indices (Bonferroni corrected for multiple comparison) was performed for each couple of models assessed;
- precision of the parameter estimates in terms of Coefficient of Variation (CV);
- visual inspection of the model fits and weighted residuals to check whether the models properly describe the data and the assumptions on the measurement error are met.

## 3.2 Results

Convoluted models (either Feng's or tri-exponential) consistently reached the lowest AIC index for all the datasets considered compared to their standard version (Figure 3.1). These differences were statistically significant according to the paired t-test on the AIC indices (Bonferroni corrected for multiple comparison) for all datasets but [$^{18}$F]FDG (Table 3.2).

When compared Feng convoluted against the tri-exponential convoluted model, the first reached significantly lower AIC for [$^{11}$C]NOP-1A, [$^{11}$C](*R*)-rolipram and [$^{11}$C]PBR28. For the remaining datasets, differences were not statistically significant.

Table 3.2: *p-value from paired t-test on AIC indices. The symbol * indicates that the difference in the AIC values were significant, i.e. p-value < 0.0083 (Bonferroni threshold).*

| Tracer | Feng vs Tri-exp | Feng vs Feng conv | Feng vs Tri-exp conv | Tri-exp vs Feng conv | Tri-exp vs Tri-exp conv | Feng conv vs Tri-exp conv |
|---|---|---|---|---|---|---|
| [$^{11}$C]MePPEP | * | * | * | * | * | 0.22 |
| [$^{11}$C]NOP-1A | 0.06 | * | * | * | * | * |
| [$^{11}$C](*R*)-rolipram | * | * | * | * | * | * |
| [$^{11}$C]PBR28 | 0.50 | * | * | * | * | * |
| L-[1-$^{11}$C]leucine | 0.03 | * | * | * | * | 0.08 |
| [$^{18}$F]FDG | 0.33 | 0.04 | 0.34 | 0.02 | 0.83 | 0.02 |
| [$^{11}$C]PiB | * | * | * | * | * | 0.30 |
| [$^{11}$C]DASB | 0.04 | * | * | * | 0.01 | 0.35 |

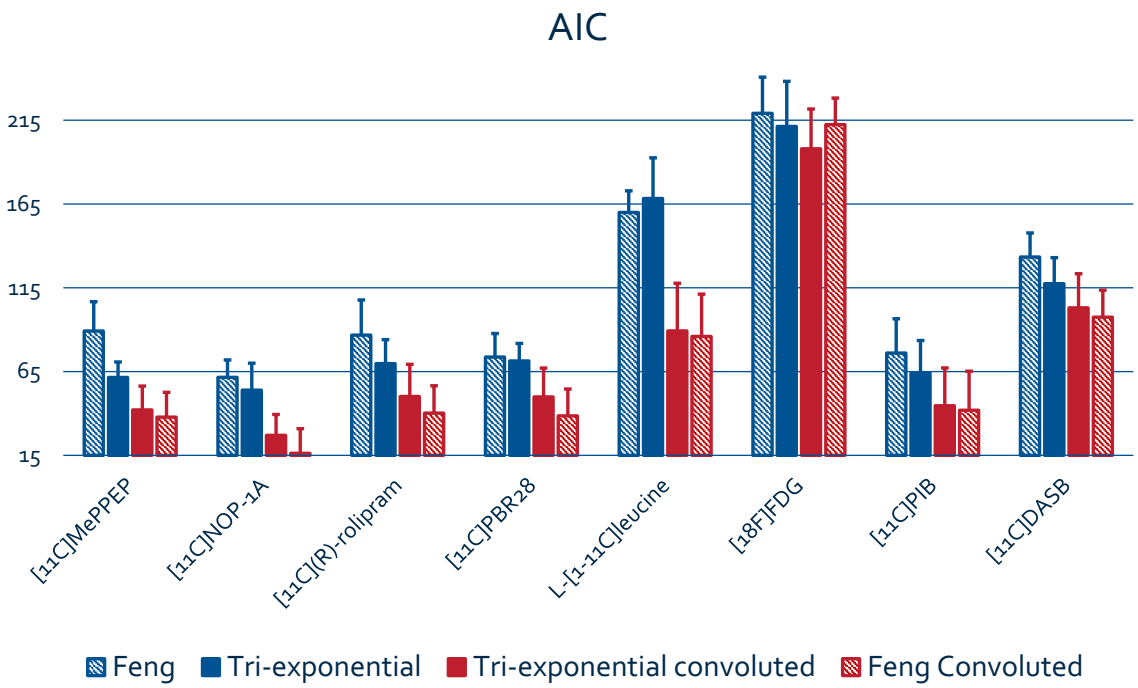


Figure 3.1: *Mean and standard deviation of the Akaike Information Criterion for each model and each dataset (the lower, the better)*

In terms of visual inspection of model fits, both convoluted models provided comparable good description of the $C_p$ measurements (Figure 3.2). No significant differences between the models in terms of weighted residuals were found. As regard the performance of the standard models, Feng's model often underestimated the peak of the radiotracer concentration while the tri-exponential model provided a very poor description of the rising phase of the $C_p$, in particular when the injection time was longer than 60 seconds (e.g. L-[1-$^{11}$C]leucine, Figure 3.2).

When considering [$^{18}$F]FDG, all models performed similarly, as already confirmed by the AIC analysis.

As regard the precision of the parameter estimates, all models had reliable parameter CVs ($< 100\%$) except for the slowest exponent in Feng's model (both $A_3$ and $a_3$ of Equation 1.12) which was often poorly estimated. A limited number of subjects across the datasets was excluded from the comparison due to the non-convergence of the estimator (maximum 7% in [$^{18}$F]FDG dataset).

## 3.3 Discussion

Taking into account the experimental protocol (i.e. the length of radiotracer injection) always improved the AIF description. This effect was particularly evident

with longer injection times ($T \geq 60s$), which is common practice in the majority of PET studies, but it was still present even for shorter protocols ($T = 20s$ and $T = 30s$, as in [$^{11}$C]PiB] and [$^{11}$C]DASB).

As regard the model selection, Feng convoluted model better performed compared to the tri-exponential convoluted model in terms of parsimony criterion, even though this difference was significant only in 3 datasets out of 8 (for [$^{11}$C]NOP-1A, [$^{11}$C](*R*)-rolipram, and [$^{11}$C]PBR28). Moreover, when we considered the $yC_p$ model description, weighted residuals and precision estimates, no clear differences could be detected, as both models behaved similarly.

In conclusion, including the injection duration in the $yC_p$ model description allows convoluted models to better describe the data compared to standard models. This approach has general applicability to all dynamic PET studies as it is not related to the particular tracer metabolism or the system physiology but it depends only on the experimental protocol of the exam. Notably these approaches do not increase model complexity, since the duration of the injection is a priori known.

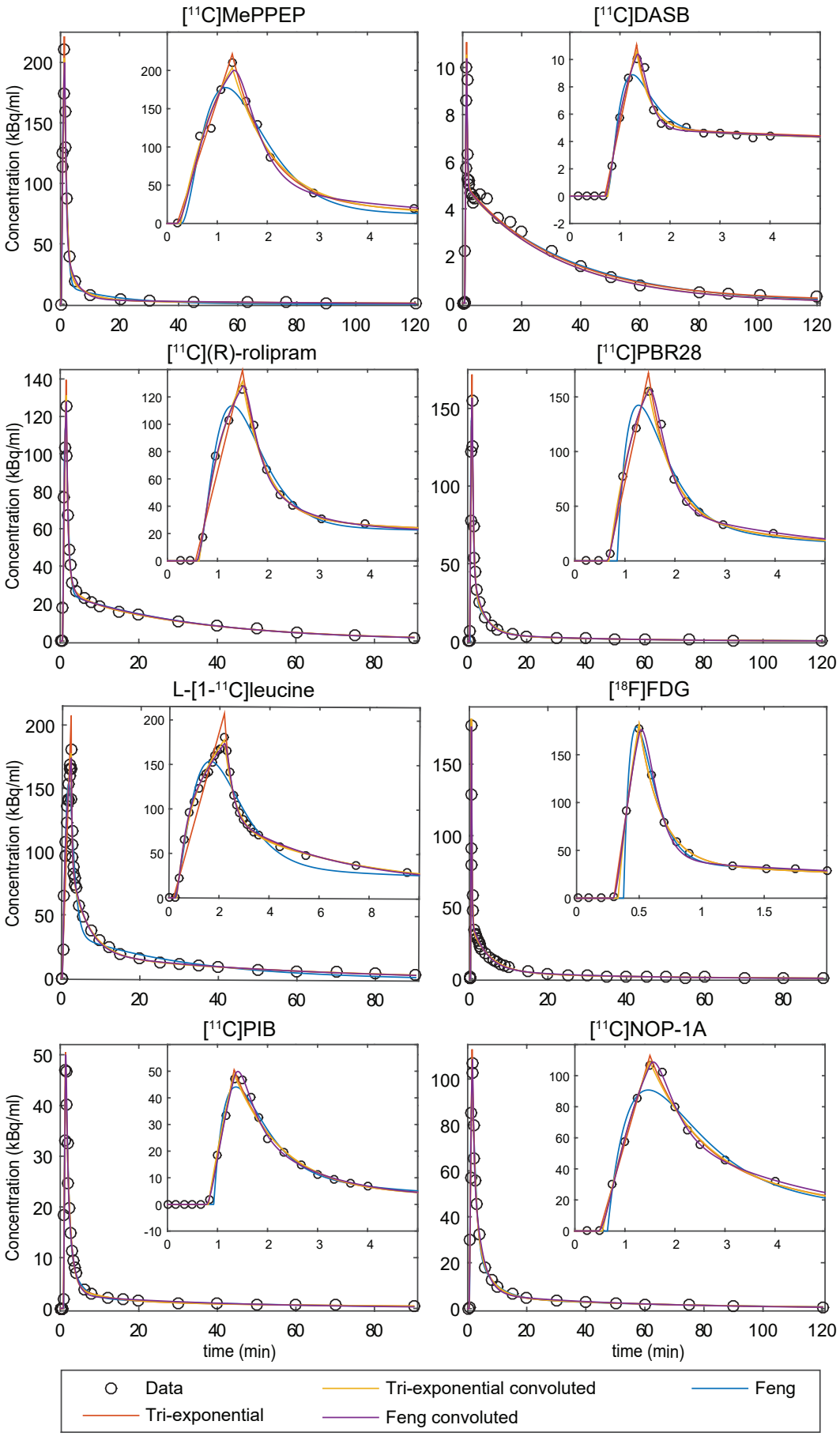


Figure 3.2: *Models fit comparison in a representative case for each dataset*

Chapter 4

# A Unified Framework For The Automatic Input Function Estimation

The aim of this chapter is to develop and validate a unified framework for the plasma data modeling, which is both biologically and experimentally informed. The approach used in the previous chapter for the modeling of the arterial input function is extended also for the radiometabolites without focusing on any tracer in particular. Given the different arterial sampling procedures employed worldwide, an estimation algorithm is also developed which is able to adapt the complexity of the model to the data available (manual versus automatic samples) by borrowing ideas from the spectral analysis [36] and basis pursuit techniques [77] already applied in PET. Furthermore, the algorithm is designed in order to require minimal interaction from the user as most of initial parameters are derived from the data itself. This approach is tested on four different tracers ([$^{11}$C]PBR28, [$^{11}$C]MePPEP, [$^{11}$C]WAY-100635 and [$^{11}$C]PiB) with automatic and manual blood sampling.

## 4.1 Materials and methods

### 4.1.1 Models of plasma input and radiometabolite data

In this section the important equations of the input function model presented in the previous chapter are reported. The same approach is then applied to the model of the radiometabolites. Moreover, it is shown how to estimates both models using basis pursuit methods.

**Plasma input function model: theory**

The theory behind the model of the input function was presented in section 3.1.1. Here we report the important equations. The model of the input function is given by:

$$yC_p(t) = \begin{cases} 0 & t \leq t_0 \\ h_p(t - t_0) * u(t) & t > t_0 \end{cases} \tag{4.1}$$

where

$$h_p(t) = \sum_{i=1}^{N} A_i e^{-a_i t} \tag{4.2}$$

and

$$u(t) = \begin{cases} 0 & t < 0 \vee t > T \\ \frac{1}{T} & 0 \leq t < T \end{cases} \tag{4.3}$$

**Plasma input function model: estimation**

In Equation 4.1 and 4.2 , the unknown variables to be estimated are the number of exponential functions $N$, their coefficients $A_i$, their exponents $a_i$, the tracer injection duration $T$ if unknown and the delay $t_0$.

This problem shares some similarities with the dynamic PET quantification problem solved by spectral analysis technique [36]: instead of fitting the nonlinear model for increasing values of $N$, one can generate a grid of many ($N > 100$) possible values for $a_i$, calculate the convolution $e^{-a_i(t-t_0)} * u(t)$ for all the pre-selected components, and then use a constrained linear optimization algorithm to estimate the coefficients $A_i$.

In standard spectral analysis the identification of a unique solution is obtained by constraining the $A_i$ coefficients to be non-negative. This approach guarantees the identification of a sparse solution (where most of the $N$ values of $A_i$ are returned as zero) but at the same time limits the method applicability to those systems without cycling connections [78]. Unfortunately this is not the case for the blood circularity system [60]. Nevertheless some assumptions can be taken to solve Equation 4.1: from both theoretical [60] and empirical evidence [79], it is known that the sum of all the $A_i$ coefficients of the IRF equals zero, with $A_i > 0$ for each coefficient except the one associated with the highest exponent (hereby

called $a_0$). The existence of a negative coefficient would prevent the use of a non-negative least square (NNLS) estimator. However, we can re-write the impulse response function with all positive coefficients as follows:

$$h_p(t) = \sum_{i=1}^{N} A_i e^{-a_i t} - A_0 e^{-a_0 t} \tag{4.4}$$

where $A_0$ is the module of the negative coefficient associated to $a_0$, $A_i > 0$, $a_0 > a_i$.

Since we imposed that the sum of all coefficients equals zero, it follows that $A_0 = \sum_{i=1}^{N} A_i$. Thus, we can write:

$$h_p(t) = \sum_{i=1}^{N} A_i \left(e^{-a_i t} - e^{-a_0 t}\right) \tag{4.5}$$

and the model for the input function $yC_p$ of Equation 4.1 becomes:

$$yC_p(t) = \begin{cases} 0 & t \leq t_0 \\ \sum_{i=1}^{N} A_i \left(e^{-a_i(t-t_0)} - e^{-a_0(t-t_0)}\right) * u(t) & t > t_0 \end{cases} \tag{4.6}$$

with $A_i > 0$ and $a_0 > a_i$.

Given $t_0$, $T$ and $a_0$, one can generate a grid of $N$ values of $a_i$ from 0 to $a_N < a_0$, compute the terms $\left(e^{-a_i(t-t_0)} - e^{-a_0(t-t_0)}\right) * u(t)$ and use a weighted non-negative optimization algorithm to estimate a sparse solution for $A_i$ (the convolution can be solved analytically, see Appendix A.1).

In this way we solved the issue of estimating the number of exponential functions to be used, the values of their coefficients and their exponents, as they are automatically inferred from the data by the NNLS estimator.

In some cases, the NNLS algorithm can select two adjacent bases. These are known as double lines and are due to the discrete nature of the $a_i$ grid: the "real" $a_i$ is not present in the grid, thus the NNLS splits the element in two adjacent parts. Under the assumption that consecutive elements result from this phenomenon, we replaced them with a single element whose coefficient was calculated as the sum of the two adjacent coefficients and the exponent was calculated as the average between the two adjacent exponents weighted for their respective coefficient,

as done in [68]:

$$A_{new} = A_i + A_{i+1} \tag{4.7}$$

$$a_{new} = \frac{a_i A_i + a_{i+1} A_{i+1}}{A_i + A_{i+1}} \tag{4.8}$$

In practice $t_0$, $T$ and $a_0$ are unknown and must be estimated before the NNLS estimator could be applied.

As regard the delay term $t_0$, we relied on the method presented in [80] by Muggeo to find break-points when fitting piecewise terms in regression models. Briefly, the rising part of the input function was modeled with a flat (zero) line from from $t = 0$ to $t = t_0$ and a straight line from zero at $t = t_0$ to $C_p(t_{peak})$ at $t = t_{peak}$, where $t_{peak}$ is the time of the input function peak. The method of Muggeo consists in an iterative algorithm to estimate the breakpoint $t_0$ of piecewise linear models and, under the assumption that such breakpoint exists, it is guaranteed to converge to the optimal solution in a finite number of steps (see appendix B.1).

As regard the injection duration $T$, this is usually known from the experimental protocol. However, in case of manual injections, the duration is susceptible to intra- and inter-operator variability and $T$ has to be estimated. It can be shown that under the assumption that $a_0$ is large, the injection time can be approximated as $T \approx t_{peak} - t_0$ (see appendix B.2 for the mathematical derivation).

For the last parameter $a_0$, we propose the use of a grid search over a range of possible values. For each candidate value, $C_p$ is fitted with the model in Equation 4.6 using a weighted NNLS algorithm as $yC_p = NLLS(C_p, t_0, T, a_0)$, where $t_0$ and $T$ are estimated as above. The value for $a_0$ is selected as the one returning the minimum Weighted Residual Sum of Squares (WRSS).

Finally, the three parameters ($t_0$,$T$,$a_0$) can be further refined using a gradient descent algorithm, as for example the Levenberg-Marquardt.

**Radiometabolite model: theory**

In [33] it was proposed to model the appearance of radiometabolites with a compartmental model whose input is the concentration of the parent, i.e. the unchanged tracer, and the outputs are the concentrations of the various radiometabolites produced.

The major drawbacks of this model is that one needs to know both the compartmental structure, which is tracer specific, and the concentration of each radiometabolite in plasma. In general, HPLC analyses are optimized to separate the parent from the radiometabolites and not to isolate multiple different radiometabolites. This last issue can be solved by lumping all the radiometabolites compartments in a single one, as done in [34].

As regard the model structure instead, since a compartmental model is a special case of a LTI system, it is always possible to write its system impulse response as a sum of exponential functions:

$$h_{met}(t) = \sum_{j=1}^{M} B_j e^{-\beta_j t} \tag{4.9}$$

Thus the concentration of all the radiometabolites lumped together ($C_{met}$) can be modeled as:

$$yC_{met} = \begin{cases} 0 & t \leq t_0 + t_1 \\ h_{met}(t - t_1) * yC_p(t) & t > t_0 + t_1 \end{cases} \tag{4.10}$$

where $t_1$ is an optional parameter which represents the delay with which the radiometabolites appear in plasma.

This system describes the metabolism of the parent concentration in plasma and it is independent from the compartmental structure (and thus from the tracer).

**Radiometabolite model: estimation**

As for the plasma input model, the model solution requires to estimate the number of exponential functions $M$, their coefficients $B_j$ and their exponents $\beta_j$ (Equation 4.9 and 4.10).Opposite to the input function model case, there is no *a priori* knowledge on the positivity of the coefficients $B_j$. However, we can still generate a grid of possible exponents $\beta_j$, calculate the basis $e^{-\beta_j(t-t_1)} * yC_p(t)$ for each of them and then employ a sparse algorithm to obtain an estimation of how many basis are necessary, along with their exponent values and coefficients (positive or negative).

The estimator chosen for this study was the Sparse Bayesian Learner (SBL) [81], already used in PET kinetic analysis [77]. Very briefly, the method imposes

a Gaussian prior with zero mean for all the coefficients $B_j$. The variance of each prior is estimated from the data and, if a base is not necessary, this becomes very small, shrinking the estimate of the associated $B_j$ towards zero. The method is fully automated and it does not require to set parameters controlling the amount of sparsity in the solution (as opposed to other sparsity estimator, as for example LASSO [82]).

The additional model parameter $t_1$, controlling the delay of radiometabolites arrival respect to the input function, can be estimated using gradient descend algorithm at the top of the SBL algorithm, as for the input function model.

### 4.1.2 Complete pipeline for plasma data modeling

The models presented above describe the time-course of $C_p$ and $C_{met}$. However, the data available from a PET experiment are usually $C_{tot}$ and $PPf$. The relation between them is:

$$C_{tot}(t) = C_p(t) + C_{met}(t) \tag{4.11}$$

$$PPf(t) = \frac{C_p(t)}{C_p(t) + C_{met}(t)} \tag{4.12}$$

In this section we will present the complete pipeline, that starting from the raw data of $C_{tot}$ and $PPf$ returns the model of the input function $yC_p$ to be used for PET tissue quantification.

For the sake of clarity, the dependence from time was dropped in this paragraph. The steps involved to estimate the input function $yC_p$ from $C_{tot}$ and $PPf$ measurements are represented in Figure 4.1.

i An initial approximation of the input function is calculated as:

$$C_p^{init} = C_{tot} \cdot lin(PPf) \tag{4.13}$$

where the operator $lin(\cdot)$ is the linear interpolation.

ii $C_p^{init}$ is fitted with the input function model described in Equation 4.6, obtaining $yC_p^{init}$. The weights $wC_p^{init}$ are derived from the law of uncertainty propagation assuming $lin(PPf)$ error-free (see Appendix C.3):

$$wC_p^{init} = \frac{wC_{tot}}{lin(PPf)^2} \tag{4.14}$$

iii An approximation of the radiometabolite concentration is derived as (from Equations 4.11 and 4.12):

$$C_{met} = yC_p^{init} \cdot \frac{1 - PPf}{PPf} \tag{4.15}$$

iv $C_{met}$ is fitted with the $yC_{met}$ model of Equation 4.10, using $yC_p^{init}$ derived from step (ii). The weights $wC_{met}$ are derived from the law of uncertainty propagation, assuming $yC_p^{init}$ error free (see Appendix C.4):

$$wC_{met} = \left(\frac{PPf^2}{yC_p^{init}}\right)^2 \cdot wPPf \tag{4.16}$$

v The model for the plasma parent fraction is calculated from $yC_p^{init}$ and $yC_{met}$ (from step ii and iv) by:

$$yPPf = \frac{yC_p^{init}}{yC_p^{init} + yC_{met}} \tag{4.17}$$

vi The discrete input function is generated from the raw $C_{tot}$ data and the estimated $yPPf$ as:

$$C_p = C_{tot} \cdot yPPf \tag{4.18}$$

vii As last step, $C_p$ is fitted with the input function model of Equation 4.6, obtaining the definitive input function $yC_p$. The weights are calculated assuming $yPPf$ to be error-free (see Appendix C.3):

$$wC_p = \frac{wC_{tot}}{yPPf^2} \tag{4.19}$$

In this last step the nonlinear parameters $t_0$, $T$ and $a_0$ can be set to the values found at the first step or refined again.

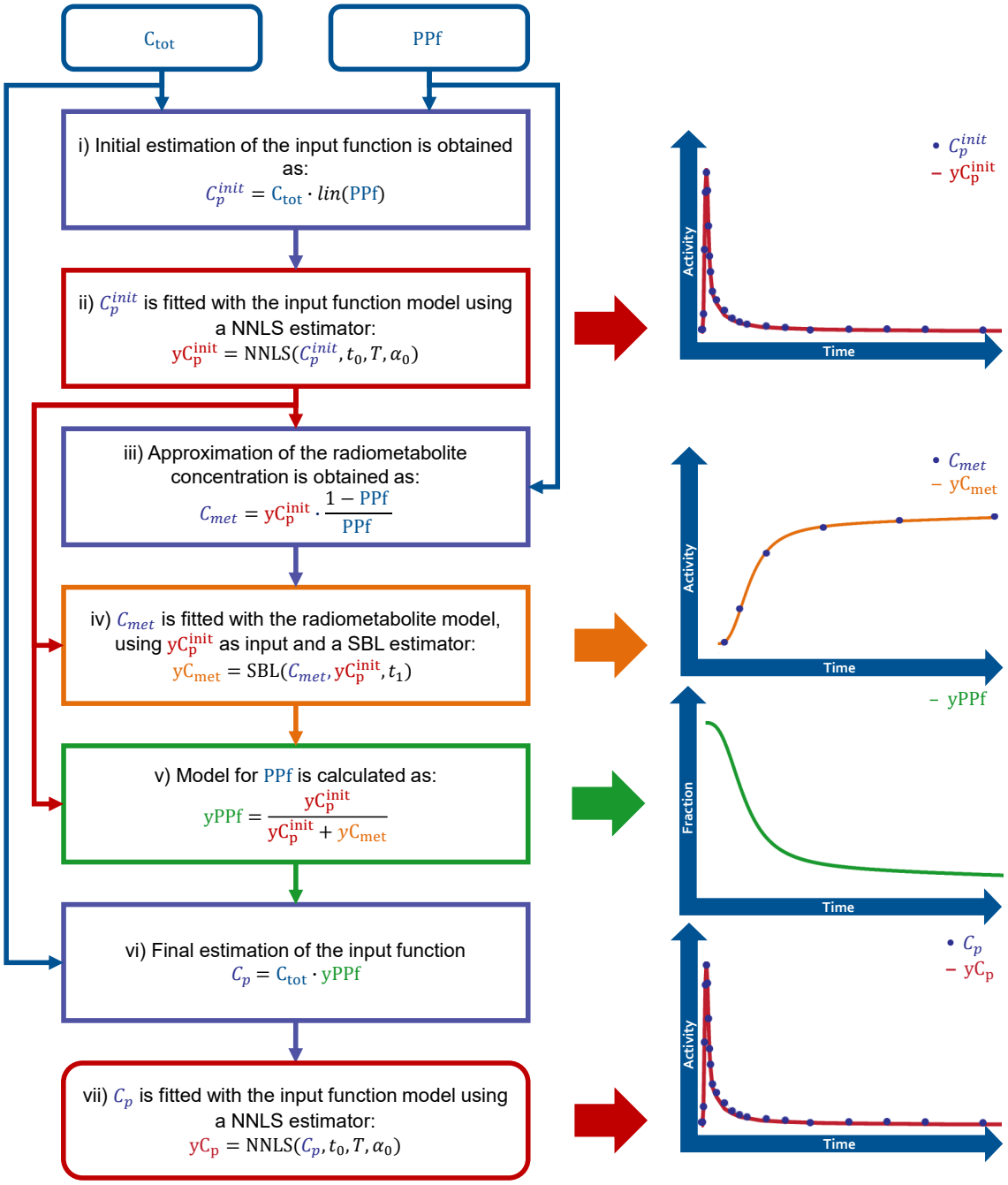


Figure 4.1: *Flowchart representing the complete pipeline for plasma data modeling. The pipeline takes as input the raw $C_{tot}$ and PPf and returns a modeled $yC_p$ ready to be used for the tissue quantification and it is fully automated. A complete explanation of each step is detailed in the main text.*

### 4.1.3 Dataset

The automatic pipeline was tested on four different datasets, two with manual ([$^{11}$C]WAY-100635 and [$^{11}$C]PiB) and two with automatic blood samples ([$^{11}$C](*R*)-rolipram and [$^{11}$C]MePPEP).

- The [$^{11}$C]WAY-100635 dataset was composed by dynamic brain PET images and blood samples of 16 healthy subjects. Details of the acquisition were described in [14]. Briefly, $C_{tot}$ was measured on 35 samples per subject collected every 5 seconds with a fraction collector system for the first 2 minutes, and manually thereafter at longer intervals. *PPf* was instead measured on 7 samples at times 1, 2, 5, 10, 30, 60 and 90 min after the tracer injection. Brain images were segmented in 16 different regions of interest (ROIs).

- The [$^{11}$C]PiB dataset was composed by 20 healthy subjects from a previous study [75]. For each subject, $C_{tot}$ was measured on 29 arterial samples extracted by pump every 10 sec for 2 min and then every 20 sec for 2 min, followed by manual draws at 6, 12, 20, 30, 40, 50, 60, 80 and 90 min after injection. PPf was measured on the 7 samples taken at times 2, 6, 12, 20, 40, 60 and 90 min. Brain images were segmented in 22 different ROIs.

- The [$^{11}$C]PBR28 dataset was composed by 19 healthy subjects from a previous study [83]. Whole blood concentration, $C_b$, was measured with an automated blood sampling system equipped with an online detector at a rate of 1 sample per second for the first 15 min. Manual samples were drawn at times 5, 10, 15, 20, 25, 30, 40, 50, 60, 70, 80 and 90 min from which $C_{tot}$ was measured. The *POB*, as ratio between $C_{tot}$ and $C_b$ in these 12 samples, was fitted using an extended Hill model (Equation 1.7) and used to correct the automatic *Cb* measurements for the non-plasmatic contribute, thus estimating $C_{tot}$ for all samples. *PPf* was measured on the 8 manual samples taken at times 5, 10, 15, 20, 30, 50, 70 and 90 min. Brain images were segmented in 215 different ROIs.

- The [$^{11}$C]MePPEP was composed by 6 healthy subjects who were part of an ongoing study aiming to investigate the role of cannabinoid receptors in schizophrenia. Whole blood concentration, $C_b$, was measured as for [$^{11}$C]PBR28 with an automated blood sampling system equipped with an online detector at a rate of 1 sample per second for the first 15 min. Manual samples were drawn at times 2, 5, 10, 15, 20, 25, 30, 40, 50, 60, 70, 80 and 90 min from which $C_{tot}$ was measured. *POB* correction was performed using an extended Hill model as before while *PPf* was measured on the 8 manual

samples taken at times 2, 5, 10, 20, 30, 50, 70 and 90 min. Brain images were segmented in 215 different ROIs.

### 4.1.4 Pipeline implementation settings

The 4 datasets were all analyzed using the same settings for the automatic pipeline: as regard the input function model, $t_0$, $T$ and $a_0$ were initialized as described above. The grid search for the initial value of $a_0$ was composed of 20 values log-spaced from 1 min $^{-1}$ to 50 min$^{-1}$ (note that this grid is used only to find the initial value of $a_0$ that will be further refined by the gradient descent algorithm). The $a_i$ grid was composed by 500 elements log-spaced from 0 min$^{-1}$ to $0.99 \cdot a_0$ min$^{-1}$. The $\beta_j$ grid was instead composed by 100 elements log-spaced from 0 min$^{-1}$ to 0.5 min$^{-1}$. The NNLS estimator used was part of the standard linear algebra function implemented in MATLAB® (www.mathworks.com). The SBL estimator is freely available at http://www.miketipping.com/downloads.htm.

Both $C_{tot}$ and $PPf$ were assumed to be corrupted by additive independent Gaussian noise with zero mean and variance known up to a proportionally constant. As regard $PPf$, the variance of the noise was assumed uniform for all measurements (data of the radiochromatogram were not available), while for $C_{tot}$ we assumed the variance proportional to its value (see Appendix C.2). Weights were then chosen as the inverse of the variance, i.e. $wPPf(t) = 1$ and $wC_{tot}(t) = C_{tot}(t)^{-1}$. For [$^{11}$C]PBR28 and [$^{11}$C]MePPEP, to avoid overfitting of the initial part of the curve due to the much higher number of automatic samples in the first 15 minutes, the weights of the automatic samples were normalized such that their sum was equal to the sum of the weights of the manual samples. In this way, automatic and manual samples gave the same contribute to the data fit.

### 4.1.5 Method evaluation

Our automatic algorithm was tested against the standard pipeline, consisting into fitting a tracer-dependent mathematical model for $PPf$ and the standard model for $C_p$, i.e. a straight line from $t_0$ to the peak followed by a tri-exponential decay (Equation 1.13). The weights were defined as for the automatic method.

For the standard method, $PPf$ data of [$^{11}$C]PiB, [$^{11}$C]PBR28 and [$^{11}$C]MePPEP were fitted with an extended Hill model (Equation 1.7), while for [$^{11}$C]WAY-100635 we used the standard Hill model (Equation 1.6) as suggested in [14]. The input function data were derived by multiplying $C_{tot}$ data with the estimated $yPPf$, and

fitted with the standard model (Equation 1.13). The value of $t_0$ was estimated with the Muggeo technique as in the automatic method.

We compared the automatic pipeline vs. the standard method on two different levels of analysis. First, the model descriptions of the plasma data obtained with the two methods were analyzed in terms of weighted residuals, that had to be uncorrelated with zero mean, following the assumptions on the model error. We applied the Wald–Wolfowitz runs test for the randomness of the residuals and the one sample t-test for the value of the mean that has to be equal to zero.

Then, we evaluated the impact of the input function derived by automatic and standard method on the tissue quantification estimates. We fitted a two tissue compartmental model with both input functions to all the ROIs for [$^{11}$C]WAY-100635, [$^{11}$C]PiB and [$^{11}$C]MePPEP, and a two tissue compartmental model with vascular trapping [84] for [$^{11}$C]PBR28. For each ROI, we compared the WRSS obtained with both input functions by calculating the percentage relative difference (RD) respect to the arithmetic mean, that is:

$$RD = 200 \cdot \frac{WRSS_{aut} - WRSS_{stan}}{WRSS_{aut} + WRSS_{stan}} \tag{4.20}$$

where $WRSS_{aut}$ and $WRSS_{stan}$ are the WRSS obtained with the automatic and standard input function respectively. The percentage relative difference respect to the arithmetic mean was also calculated for the volume of distribution $V_T$ and the binding potential $BP_{ND}$, defined from the model micro-parameters as in [66]. Relative differences on model micro-parameters were also included in the comparison. Sign test was used to detect if these were significantly different from zero.

## 4.2 Results

### 4.2.1 Plasma data analysis

The automated pipeline accurately described the plasma data in all the subjects of the four datasets, regardless the presence of manual or automatic samples. An example of the method performances obtained for each tracer is reported in Figure 4.2. The peak of $C_{tot}$ was well described in both its rising and decreasing phase and the *PPf* was correctly modeled (zoomed images in all panels). The median number of exponential function used to fit $C_p$ was 5 for [$^{11}$C]WAY-100635 and [$^{11}$C]PiB, 6 for [$^{11}$C]PBR28 and 4 for [$^{11}$C]MePPEP. The median number of

exponential functions used to fit $C_{met}$ was instead 2 for [$^{11}$C]WAY-100635 and 3 for the other tracers.

There were no differences in the *PPf* description with the automatic pipeline and the standard method: the *PPf* weighted residuals were uncorrelated and consistent with the assumptions on the measurement error in both cases. When considering the weighted residuals of $C_{tot}$ instead, the automatic pipeline outperformed the standard method (Table 4.1). For [$^{11}$C]WAY-100635 and [$^{11}$C]PiB (manual sampling), the weighted residuals were in agreement with the measurement error assumptions for all the subjects when using the automatic pipeline. On the contrary, 63% and 50% of the subjects showed correlated weighted residuals when using the standard pipeline. The same held for [$^{11}$C]PBR28 (automatic samples): when using the standard method, most of the subjects failed either the randomness test or the t-test, while for the automatic pipeline only 4 out of 19 subjects had non-random weighted residuals. [$^{11}$C]MePPEP was the most challenging dataset: both with the automatic and standard pipeline the majority of the subjects presented correlated residuals. However, the automatic pipeline still outperformed the standard method, since for the latter 4 out of 6 subjects failed the t-test on residuals mean.

Table 4.1: *$C_{tot}$ weighted residuals analysis: table shows the number of subjects for which the Wald-Wolfowitz runs test (for correlated residuals) and the t-test (for mean different from zero) found deviations from the error model assumptions. Results are reported separately for the automatic or standard pipeline*

| | | Automatic pipeline | | Standard pipeline | |
|---|---|---|---|---|---|
| Tracer | N | Correlated residuals | Mean ≠ 0 | Correlated residuals | Mean ≠ 0 |
| [$^{11}$C]WAY-100635 | 16 | 0 | 0 | 10 | 2 |
| [$^{11}$C]PiB | 20 | 0 | 0 | 10 | 0 |
| [$^{11}$C]PBR28 | 19 | 4 | 0 | 13 | 12 |
| [$^{11}$C]MePPEP | 6 | 4 | 0 | 5 | 4 |

### 4.2.2 Impact on tissue data quantification

The use of the input function obtained with the automated pipeline significantly improved the tissue data description for all the tracers considered except [$^{11}$C]PBR28 (Table 4.2). In more details, the WRSS relative difference showed a median improvement of $-4\% \pm 21\%$ ($p = 0.004$) for [$^{11}$C]WAY-100635; $-14\% \pm 31\%$ ($p < 0.001$) for [$^{11}$C]PiB and $-5\% \pm 12\%$ ($p < 0.001$) for [$^{11}$C]MePPEP. There was no difference in the WRSS for [$^{11}$C]PBR28 ($-0.005\% \pm 24\%$, $p = 0.96$).

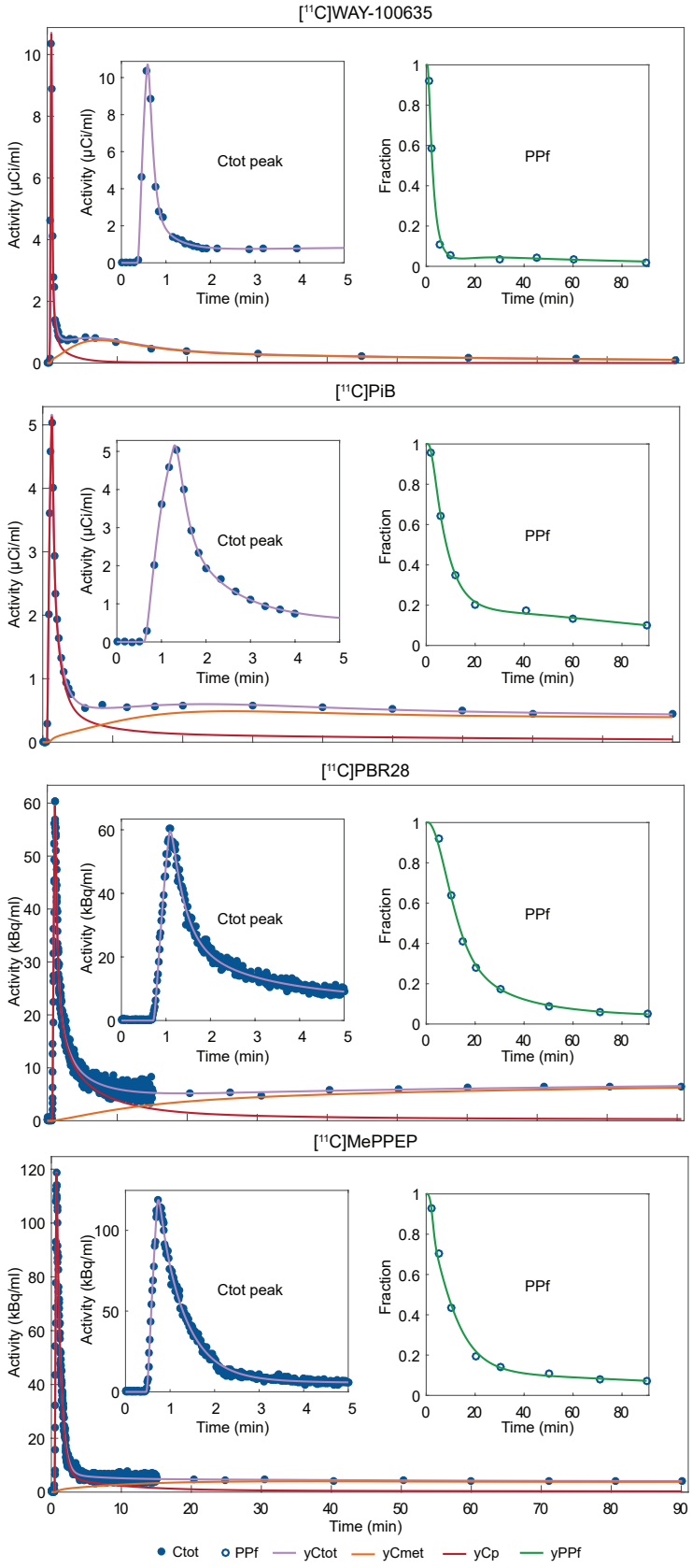


Figure 4.2: *Examples of plasma data fit for a representative subject of each tracer obtained with the automatic pipeline.*

The impact on the macro-parameter estimates of $V_T$ was significant for all the tracers but [$^{11}$C]PBR28, for which it was $-0.016\% \pm 6\%$ ($p = 0.93$). The differences ranged from $-8\% \pm 9\%$ ($p < 0.001$) for [$^{11}$C]WAY-100635 to $5\% \pm 3\%$ ($p < 0.001$) for [$^{11}$C]MePPEP. As regard the binding potential $BP_{ND}$, estimates were statistically different only with the automatic sampled datasets: $-24\% \pm 13\%$ ($p < 0.001$) for [$^{11}$C]PBR28 and $-13\% \pm 25\%$ ($p < 0.001$) for [$^{11}$C]MePPEP. Micro-parameters were also affected by the input function modeling for all the tracers considered (Table 4.2).

Table 4.2: *Impact of the plasma data processing pipeline on tissue estimates. The impact on the tissue quantification is reported as relative differences between the kinetic parameters obtained using the input function derived with the automatic pipeline and those obtained with the input function derived with the standard pipeline. The relative difference on the tissue WRSS is also reported (when negative, the input function from the automatic pipeline produced a better description of the tissue data, i.e. lower WRSS). * $p < 0.05$*

| | Relative difference (median ± median absolute deviation) | | | | | | | | |
|---|---|---|---|---|---|---|---|---|---|
| Tracer | Tissue WRSS | $K_1$ | $k_2$ | $k_3$ | $k_4$ | $k_i$ | $V_b$ | $V_T$ | $BP_{ND}$ |
| [$^{11}$C]WAY-100635 | −4± 21%* | 1± 5% | 9± 21%* | 2± 25% | 3± 10%* | | −4± 17%* | −8± 9%* | −2± 28% |
| [$^{11}$C]PiB | −14± 31%* | −10± 3%* | −8± 3%* | −19± 17%* | −20± 26%* | | 15± 22%* | −2± 8%* | −2± 19% |
| [$^{11}$C]PBR28 | 0± 24% | −3± 5%* | −18± 12%* | −32± 19%* | −9± 13%* | −45± 16%* | 36± 12%* | 0± 6% | −24± 13%* |
| [$^{11}$C]MePPEP | −5± 12%* | −1± 2%* | −17± 24%* | −28± 22%* | −13± 11%* | | 19± 9%* | 5± 3%* | −13± 25%* |

## 4.3 Discussion

In this work, we presented a unified and biologically informed framework for the plasma data modeling, which is grounded on the tracer-tracee theory. Both $yC_p$ and $yC_{met}$ models included the duration of the tracer injection in their formulation, thus taking advantage of both physiological and experimental information. Furthermore, we proposed an algorithm which requires minimal interaction with the user, making the modeling of data of different tracers acquired with different sampling modalities more robust and flexible. We tested this automatic pipeline with four different tracers acquired in two different centers: one employed an

online detector for the automatic measurement of the blood samples, the other performed manual sampling. Performance were compared against the standard modeling approach.

**Method implementation**

A key aspect in the implementation of the pipeline was the use of a sets of basis functions for identifying both $yC_p$ and $yC_{met}$ models. This allows to avoid the direct estimation of a high number of parameters in a non-linear fashion with all the related problems, such as the definition of appropriate initial estimates which may differ from tracer to tracer. The need to set the initial values is replaced by the simpler setting of just two extreme exponents for the grid of basis and of the total number of elements.

As regards the $a_i$ grid related to $yC_p$, we used 500 elements but obtained similar results with a number varying from 100 to 1000 elements (data not shown). The computational cost increased with the number of elements, but from the user standpoint this increase is negligible (few seconds) even with 1000 grid elements and the automatic sampled dataset. Nevertheless, 500 elements represent a good trade-off between estimate precision and algorithm efficiency. The grid range was simple to set as the first value can be set to 0 while the largest must be less than $a_0$: in our implementation we set it at 99% of the value of $a_0$. An important aspect of this implementation is that it allows to automatically select the number of exponents needed to describe the data. The median number of elements for $yC_p$ ranged from 4 to 6, which correspond to a much more complex model than the standard one. Since the standard model has weighted residuals that resulted correlated for most of subjects, it is probable that this model is too parsimonious to describe $C_p$ data.

Also when considering the radiometabolite model, the number of grid elements had again no impact. On the contrary, the grid range was more important: the minimum $\beta_j$ can be safely set to 0, while choosing a maximum value too high ($\beta_M > 1$) resulted in overfitting of the $C_{met}$ for a few subjects (Figure 4.3). In this case, especially at the beginning of the curve, the model highest component fits also the measurement error and results in spurious large oscillations (zoomed panel). This is not physiological but it can be easily identified by visual inspection and corrected by reducing the maximum value of $\beta_j$.

One additional advantage of this implementation is that one does not have to select an empirical function to fit the $PPf$. The model selection for the ra-

diometabolites is inherently performed by the SBL estimator when it determines the number of exponential functions to be used. In this case, the median number of elements selected by the SBL estimator for $yC_{met}$ ranged from 2 to 3, in line with the standard *yPPf* models (see Section 1.3). No deviance from the error model assumption were found with either the standard or the automatic pipeline for the description of *PPf*. However, due to the low number of samples it is possible that the tests had not enough statistical power to detect an effect.

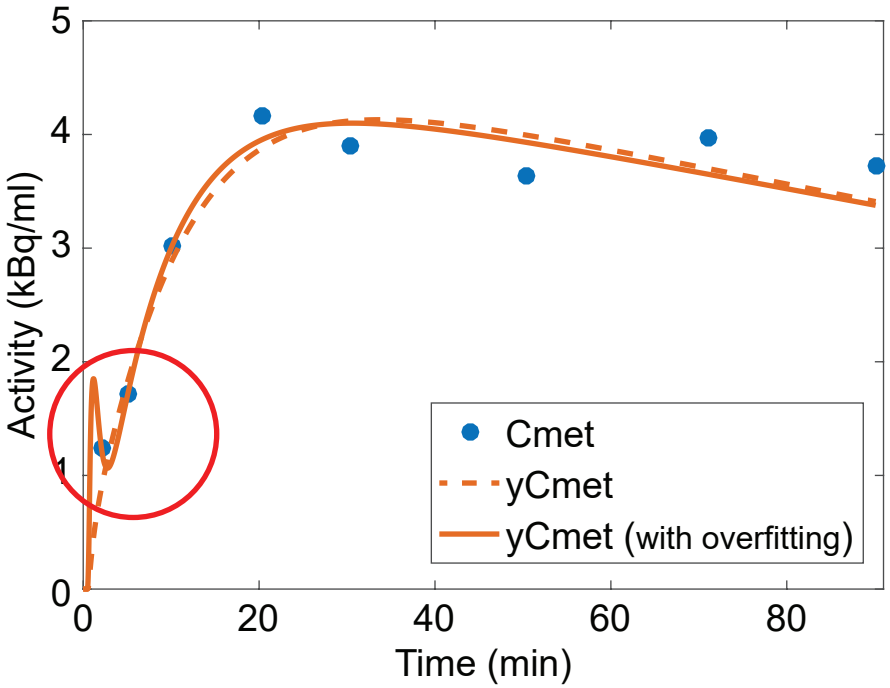


Figure 4.3: *Example of overfit in a [$^{11}$C]MePPEP subject: the $yC_{met}$ model in solid line was obtained using a maximum value of the β grid equal to $2min^{-1}$. It can be noted inside the red circle that the solid line tends to pass perfectly through the first two $C_{met}$ samples producing a large non physiological oscillation (overfitting). This effect can be easily identified and resolved by decreasing the maximum value of the β grid ($0.5min^{-1}$ for the $yC_{met}$ model in dashed line)*

**Pipeline performance**

In PET study the true input function is not known, therefore it was not possible to determine if this unified modeling approach was more accurate than the standard approach. However, as an indirect test, we first assessed whether the model descriptions of the plasma data respected the assumptions on the measurement error. Then, we fitted the tissue time activity curves using the input functions derived with both approaches and the one generated with the automatic pipeline better described the tissue data (statistically lower WRSS). Notably, the impact on the tissue parameter estimates was in general smaller for $V_T$ (in module $< 10\%$)

and higher on $BP_{ND}$ (in module up to 24%) and micro-parameters (in module up to 45%). This result was in line with the results obtained in Section 2.2.3 and other studies [13] [14] where the input function was found to be a major source of variability in the kinetic analysis of dynamic PET images.

**Efficient tissue quantification by exploiting analytical convolution**

A further advantage of the proposed input function model is that the same convolution calculated for the radiometabolite model can be used for tissue quantification, where the tissue model is $yC_T(t) = h_T(t) * yC_p(t)$, where $h_T(t)$ is a sum of decaying exponential functions [35]. Therefore, the solution of the tissue model can be implemented analytically exactly as for the radiometabolites model (see Appendix A.2). This results in a huge speedup of the computation: compared to the numerical convolution with a 1 sec integration step, the analytical form was 16 times faster. The proposed input function model can therefore reduce the computational burden of tissue quantification, especially at the voxel level.

## 4.4 Conclusion

The novel biologically informed plasma and radiometabolite models, in conjunction with the estimator algorithm here proposed, were able to provide excellent fits of the plasma data for all the four tracers considered. The method showed superior fits compared to the standard pipeline, for both manually and automatically measured blood samples. The method is fast and requires minimal interaction from the user.

# Chapter 5

# Conclusion

In this thesis, a unified framework for the plasma data modeling was derived from the principles of the tracer-tracee theory and used to describe the concentration of the tracer and its radiometabolites in plasma. Moreover, the framework incorporated the information of the tracer injection duration, resulting in a more realistic description of the tracer kinetic in plasma. Hence, the models derived were both physiologically and experimentally informed, resulting in a more accurate description of the plasma data compared to the standard models currently used in the literature for a wide range of tracers.

The choice of the models for the radiometabolites correction and the input function was shown to significantly affect the final tissue estimates, suggesting that the standard models, providing a poorer fit of the plasma data, may introduce a bias in PET quantification.

In order to promote the use of these models also in clinical practice or in those PET centers lacking proper modeling skills, an automatic pipeline for the estimation of these models was developed. This automatic pipeline took as input the raw plasma data and, requiring minimum interaction with the user, returned the model of the input function ready to be used for PET tissue quantification. Moreover, the automatic pipeline was able to correctly fit the physiological models both when automatic or manual plasma samples were available.

In conclusion, since the input function is a major source of variability in PET experiments, the methodological advancements proposed in this thesis are believed to positively impact the field, promoting a standardization of the plasma data modeling.

# Appendices

Appendix A

# Analytical expression of physiological models

## A.1 Model of the input function $yC_p$

Since the convolution is a linear operation, we can write the $yC_p$ model for $t > t_0$ as:

$$yC_p(t) = \sum_{i=1}^{N} A_i \left( e^{-a_i(t-t_0)} * u(t,T) - e^{-a_0(t-t_0)} * u(t,T) \right) \tag{A.1}$$

Thus, we just need the analytical solution of an expression of the form $\Phi(a,t) = e^{-a(t-t_0)} * u(t,T)$, which is given by:

$$\Phi(a,t) = \begin{cases} \frac{1-e^{-a(t-t_0)}}{aT} & t_0 \leq t < T + t_0 \\ \frac{e^{-a(t-t_0-T)} - e^{-a(t-t_0)}}{aT} & t \geq T + t_0 \end{cases} \tag{A.2}$$

The special case of $a = 0$ results in:

$$\Phi(0,t) = \begin{cases} \frac{(t-t_0)}{T} & t_0 \leq t < T + t_0 \\ \frac{1}{T} & t \geq T + t_0 \end{cases} \tag{A.3}$$

The final expression for the $yC_p$ model is given by:

$$yC_p(t) = \begin{cases} 0 & t \leq t_0 \\ \sum_{i=1}^{N} A_i \left( \Phi(a_i,t) - \Phi(a_0,t) \right) & t > t_0 \end{cases} \tag{A.4}$$

## A.2 Model of the radiometabolites $yC_{met}$

Similarly, we can write the model $yC_{met}$ for $t > t_0$ as:

$$yC_{met}(t) = \sum_{j=1}^{M} B_j \left[ \sum_{i=1}^{N} A_i \left( e^{-a_i(t-t_0)} * e^{-\beta_j t} * u(t,T) - e^{-a_0(t-t_0)} * e^{-\beta_j t} * u(t,T) \right) \right] \tag{A.5}$$

In this case we need the analytical solution of expressions of the form $\Psi(a,\beta,t) = e^{-a(t-t_0)} * e^{-\beta t} * u(t,T)$, which is given by:

$$\Psi(a,\beta,t) = \begin{cases} \frac{\beta\left(1-e^{-a(t-t_0)}\right)-a\left(1-e^{-\beta(t-t_0)}\right)}{a\beta(a-\beta)T} & t_0 \le t < T+t_0 \\ \frac{a\left(e^{-\beta(t-t_0-T)}-e^{-\beta(t-t_0)}\right)-\beta\left(e^{-a(t-t_0-T)}-e^{-a(t-t_0)}\right)}{a\beta(a-\beta)T} & t \ge T+t_0 \end{cases} \tag{A.6}$$

Special cases are:

$$\Psi(0,0,t) = \begin{cases} \frac{(t-t_0)^2}{2T} & t_0 \le t < T+t_0 \\ \frac{(t-t_0)^2-(t-t_0-T)^2}{2T} & t \ge T+t_0 \end{cases} \tag{A.7}$$

$$\Psi(a,0,t) = \begin{cases} \frac{e^{-a(t-t_0)}+a(t-t_0)-1}{2a^2T} & t_0 \le t < T+t_0 \\ \frac{e^{-a(t-t_0)}-e^{-a(t-t_0-T)}+aT}{2a^2T} & t \ge T+t_0 \end{cases} \tag{A.8}$$

$$\Psi(0,\beta,t) = \begin{cases} \frac{e^{-\beta(t-t_0)}+\beta(t-t_0)-1}{2\beta^2T} & t_0 \le t < T+t_0 \\ \frac{e^{-\beta(t-t_0)}-e^{-\beta(t-t_0-T)}+\beta T}{2\beta^2T} & t \ge T+t_0 \end{cases} \tag{A.9}$$

$$\Psi(a,a,t) = \begin{cases} \frac{1-e^{-a(t-t_0)}(1+a(t-t_0))}{a^2T} & t_0 \le t < T+t_0 \\ \frac{e^{-a(t-t_0-T)}(1+a(t-t_0-T))-e^{-a(t-t_0)}(1+a(t-t_0))}{a^2T} & t \ge T+t_0 \end{cases} \tag{A.10}$$

To note, in case one wants to include also the optional parameter $t_1$ in the model $yC_{met}$, he must substitute $t_0$ with $t_0 + t_1$ in all the above formulas. The final expression for the $yC_{met}$ model is given by:

$$yC_p(t) = \begin{cases} 0 & t \le t_0 \\ \sum_{j=1}^{M} B_j \left[ \sum_{i=1}^{N} A_i \left( \Psi(a_i,\beta_j,t) - \Psi(a_0,\beta_j,t) \right) \right] & t > t_0 \end{cases} \tag{A.11}$$

# Appendix B

# Initial parameters for $yC_p$

## B.1 Estimation of $t_0$

The Muggeo method [80] allow to find break-points when fitting linear piecewise terms in regression models. Considering the following model:

$$y(t) = at + b(t - t_0)H(t - t_0) \tag{B.1}$$

where $t_0$ is the break-point we want to estimate; $H(t - t_0)$ is the Heaviside step function, i.e. $H(t) = 1$ for $t > 0$, 0 otherwise; $a$ is the slope of the first segment, from $t = 0$ to $t = t_0$ and $b$ is the difference in slope between the left and the right segment, i.e. the slope for $t > t_0$ is given by $a + b$.

We want to fit this model to the first part of $C_p$, for $t \leq t_{peak}$. In other words, we approximate the rising part of the curve with two linear segments. The slope of the first segment will be zero, as at the beginning of $C_p$ there is no activity, thus a flat line ($a = 0$). After $t_0$, the slope will be $b$. Following the algorithm in [80], at the s-th iteration, the steps are:

- Fix $t_0^{(s)}$ and calculate two auxiliary variates:

$$U^{(s)}(t) = (t - t_0^{(s)})H(t - t_0^{(s)}) \tag{B.2}$$

$$V^{(s)}(t) = -H(t - t_0^{(s)}) \tag{B.3}$$

- Fit the following linear model to $C_p(t \leq t_{peak})$:

$$y^{(s)}(t) = \beta^{(s)}U^{(s)}(t) + \gamma^{(s)}V^{(s)}(t) \tag{B.4}$$

- Improve the break-point estimate:

$$t_0^{(s+1)} = \frac{\gamma^{(s)}}{\beta^{(s)}} + t_0^{(s)} \tag{B.5}$$

- Repeat until convergence.

The algorithm was initialized with $t_0^{(1)} = 0.5 \cdot t_{peak}$ and convergence criteria was set as $\mid \gamma^{(s)} \mid < 1E-6$. For all subjects, algorithm converged in less than 10 iterations.

## B.2 Estimation of $T$

Considering the term $\Phi(a_i, t) - \Phi(a_0, t)$ of Equation A.4 for $t \geq T + t_0$. The time of its peak, $t_{peak}$, can be found imposing:

$$\frac{\mathrm{d}\left(\Phi(a_i, t) - \Phi(a_0, t)\right)}{\mathrm{d}t} = 0 \tag{B.6}$$

$$e^{-a_i(t-t_0)} - e^{-a_0(t-t_0)} - e^{-a_i(t-t_0-T)} + e^{-a_0(t-t_0-T)} = 0 \tag{B.7}$$

$$e^{-a_i(t-t_0)} \cdot (1 - e^{a_i T}) = e^{-a_0(t-t_0)} \cdot (1 - e^{a_0 T}) \tag{B.8}$$

$$-a_i\,(t - t_0) + \log(1 - e^{a_i T}) = -a_0\,(t - t_0) + \log(1 - e^{a_0 T}) \tag{B.9}$$

$$t = t_0 - \frac{\log(e^{a_i T} - 1)}{a_0 - a_i} + \frac{\log(e^{a_0 T} - 1)}{a_0 - a_i} \tag{B.10}$$

The solution has three terms: $t_0$, $\frac{\log(e^{a_i T}-1)}{a_0-a_i}$ and $\frac{\log(e^{a_0 T}-1)}{a_0-a_i}$. For $a_0 \to +\infty$, the second term goes to zero, while $\lim_{t\to\infty} \frac{\log(e^{a_0 T}-1)}{a_0-a_i} = T$. Since $a_0$ is the largest exponent, this is a fairly good approximation and the resulting solution does not include dependency from $a_i$. Thus, independently from the number and the values of the exponential functions selected from the $a$ grid, we can write $T \approx t_{peak} - t_0$ (as $a_0$ is not infinite the correct relation is $T < t_{peak} - t_0$).

# Appendix C

# Measurements error models

In this appendix the derivation of the variance associated with the measurement error of $PPf$, $C_{tot}$, $C_p$ and $C_{met}$ are presented.

## C.1 $PPf$

Starting from Equation 1.3:

$$PPf(t) = \frac{AUC_p(t)}{AUC_p(t) + AUC_{met}(t)} \tag{C.1}$$

Both $AUC_p(t)$ and $AUC_{met}(t)$ represent a sum over time of radioactive counts. These are random processes that can be approximated as Gaussian distributions whose variance is proportional to the mean. The Gaussian approximation holds well when the number of counts is "high" [76]. Thus, the variance of the two processes can be expressed as follows:

$$\mathrm{Var}(AUC_p(t)) = \gamma \cdot AUC_p(t) \tag{C.2}$$

$$\mathrm{Var}(AUC_{met}(t)) = \gamma \cdot AUC_{met}(t) \tag{C.3}$$

where $\gamma$ is the unknown proportionally constant, which is assumed equal for both $AUC_p(t)$ and $AUC_{met}(t)$ (this is an approximation as the radiometabolites are usually eluted earlier in the HPLC, thus they have a higher signal-noise ratio due to the longer radioactive decay affecting the parent peak).

To derive the variance of $PPf$, we used the formula of propagation of variance [85] that, for a function $f(x, y)$ is given by:

$$\mathrm{Var}(f) = \left[\frac{\delta f}{\delta x}\right]^2 \cdot \mathrm{Var}(x) + \left[\frac{\delta f}{\delta y}\right]^2 \cdot \mathrm{Var}(y) + 2\left[\frac{\delta f}{\delta x}\right]\left[\frac{\delta f}{\delta y}\right]\mathrm{Var}(x, y) \tag{C.4}$$

where $\mathrm{Var}(x, y)$ is the covariance between $x$ and $y$, while $\delta f/\delta x$ and $\delta f/\delta y$ are the partial derivate of $f$ with respect to $x$ and $y$ respectively.

Assuming $AUC_p(t)$ and $AUC_{met}(t)$ to be independent, their covariance was zero. Thus, the formulation of the variance of $PPf(t)$ was calculated as follows (for the sake of clarity, the dependency from the time $t$ has been omitted in the following passages):

$$\mathrm{Var}(PPf) = \left[\frac{\delta PPf}{\delta AUC_p}\right]^2 \cdot \mathrm{Var}(AUC_p) + \left[\frac{\delta PPf}{\delta AUC_{met}}\right]^2 \cdot \mathrm{Var}(AUC_{met}) \tag{C.5}$$

$$= \left[\frac{AUC_{met}}{(AUC_p + AUC_{met})^2}\right]^2 \gamma AUC_p + \left[\frac{-AUC_p}{(AUC_p + AUC_{met})^2}\right]^2 \gamma AUC_{met} \tag{C.6}$$

$$= \gamma \frac{AUC_p \cdot AUC_{met} \cdot (AUC_p + AUC_{met})}{(AUC_p + AUC_{met})^4} \tag{C.7}$$

$$= \gamma \frac{AUC_p \cdot AUC_{met}}{(AUC_p + AUC_{met})^3} \tag{C.8}$$

## C.2 $C_{tot}$

In case $C_{tot}$ is measured directly from a gamma counter, it represents a radioactive count and thus its variance can be approximated by a Gaussian distribution with variance proportional to the mean:

$$\mathrm{Var}(C_{tot}(t)) = \gamma \cdot C_{tot}(t) \tag{C.9}$$

$C_{tot}$ must be corrected for the radioactive decay, which is done multiplying the measured radioactivity per $e^{\lambda t_m}$, where $\lambda$ is the disintegration constant and it is equal to $\lambda = \ln 2/T_{1/2}$, with $T_{1/2}$ representing the isotope half-life ($T_{1/2} = 20.4min$ for $^{11}$C and $109.8min$ for $^{18}$F); and $t_m$ is the time at which the sample is measured. To note that $t_m \neq t$. The variance of $C_{tot}$ is therefore more correctly calculated as:

$$\mathrm{Var}(C_{tot}(t)) = \gamma \cdot e^{2\lambda t_m} C_{tot}(t) \tag{C.10}$$

Using this correction, the assumption that $\gamma$ is constant between different time points is less critic.

Instead, when the automatic sampler is used, $C_{tot}$ is derived from Equation 1.2:

$$C_{tot}(t) = C_b(t) \cdot yPOB(t) \tag{C.11}$$

The variance of $C_b$ is modeled as for $C_{tot}$:

$$\text{Var}(C_b(t)) = \gamma \cdot e^{2\hat{\eta}t_m} C_b(t) \tag{C.12}$$

Thus, using Equation C.4 for the propagation of variance, the variance of $C_{tot}$ when using an online sampler is calculated as:

$$\text{Var}(C_{tot}(t)) = yPOB(t)^2 \cdot \text{Var}(C_b(t)) \tag{C.13}$$

## C.3 $C_p$

$C_p$ is calculated from Equation 1.4 :

$$C_p(t) = C_{tot}(t) \cdot yPPf(t) \tag{C.14}$$

Applying the formula for the propagation of variance (Equation C.4), its variance is equal to:

$$\text{Var}(C_p(t)) = yPPf(t)^2 \cdot \text{Var}(C_{tot}(t)) \tag{C.15}$$

## C.4 $C_{met}$

$C_{met}$ is calculated from Equation 4.15 :

$$C_{met}(t) = yC_p(t) \cdot \frac{1 - PPf(t)}{PPf(t)} \tag{C.16}$$

Applying the formula for the propagation of variance (Equation C.4), its variance is equal to:

$$\text{Var}(C_{met}(t)) = \left(\frac{yC_p(t)}{PPf(t)^2}\right)^2 \cdot \text{Var}(PPf(t)) \tag{C.17}$$

Equation C.16 use the modeled input function $yC_p$ and the raw $PPf$ to calculate $C_{met}$. One can also use the raw $C_{tot}$ instead of the raw $PPf$:

$$C_{met}(t) = C_{tot}(t) - yC_p(t) \tag{C.18}$$

In this case the variance would simply be:

$$\text{Var}(C_{met}(t)) = \text{Var}(C_{tot}(t)) \tag{C.19}$$

Finally, $C_{met}$ can be calculated using only raw data as:

$$C_{met}(t) = C_{tot}(t) \cdot (1 - PPf(t)) \tag{C.20}$$

When applying Equation C.4, now both terms contribute to the final variance:

$$\mathrm{Var}(C_{met}(t)) = (1 - PPf(t))^2 \cdot \mathrm{Var}(C_{tot}(t)) - C_{tot}(t)^2 \cdot \mathrm{Var}(PPf(t)) \tag{C.21}$$

# Bibliography


[1] M. Reivich and A. Alavi, *Positron emission tomography*. New York: A.R. Liss, 1985.

[2] B. Mazoyer, "Positron Emission Tomography: Basic Principles and Potential Interest for Pharmacological Studies," in *PET for Drug Development and Evaluation*. Dordrecht: Springer Netherlands, 1995, pp. 25–35. [Online]. Available: http://www.springerlink.com/index/10.1007/978-94-011-0429-6{_}2

[3] C. Cobelli, D. Foster, and G. Toffolo, *Tracer Kinetics in Biomedical Research*. New York: Springer, 2000.

[4] R. E. Carson, "Tracer Kinetic Modeling in PET," in *Positron Emission Tomography*. London: Springer-Verlag, pp. 127–159. [Online]. Available: http://link.springer.com/10.1007/1-84628-007-9{_}6

[5] T. V. B. Greitz, D. H. Ingvar, and L. Wide, *The metabolism of the human brain studied with positron emission tomography*. New York: Raven Press, 1985.

[6] P. E. Valk, *Positron emission tomography : basic science and clinical practice*. London: Springer, 2003.

[7] A. F. Shields, D. a. Briston, S. Chandupatla, K. a. Douglas, J. Lawhorn-Crews, J. M. Collins, T. J. Mangner, L. K. Heilbrun, and O. Muzik, "A simplified analysis of [18F]3'-deoxy-3'-fluorothymidine metabolism and retention." *European journal of nuclear medicine and molecular imaging*, vol. 32, no. 11, pp. 1269–1275, 2005.

[8] V. W. Pike, "PET radiotracers: crossing the blood-brain barrier and surviving metabolism," *Trends in Pharmacological Sciences*, vol. 30, no. July, pp. 431–440, 2009.

[9] S. S. Zoghbi, H. U. Shetty, M. Ichise, M. Fujita, M. Imaizumi, J.-S. Liow, J. Shah, J. L. Musachio, V. W. Pike, and R. B. Innis, "PET imaging of the dopamine transporter with 18F-FECNT: a polar radiometabolite confounds

brain radioligand measurements." *Journal of nuclear medicine : official publication, Society of Nuclear Medicine*, vol. 47, pp. 520–527, 2006.

[10] S. E. Kim, Z. Szabo, C. Seki, H. T. Ravert, U. Scheffel, R. F. Dannals, and H. N. Wagner, "Effect of tracer metabolism on PET measurement of [11C]pyrilamine binding to histamine H1 receptors." *Annals of nuclear medicine*, vol. 13, no. 2, pp. 101–107, 1999.

[11] T. Sasaki, H. Ito, Y. Kimura, R. Arakawa, H. Takano, C. Seki, F. Kodaka, S. Fujie, K. Takahata, T. Nogami, M. Suzuki, H. Fujiwara, H. Takahashi, R. Nakao, T. Fukumura, a. Varrone, C. Halldin, T. Nishikawa, and T. Suhara, "Quantification of Dopamine Transporter in Human Brain Using PET with 18F-FE-PE2I," *Journal of Nuclear Medicine*, vol. 53, pp. 1065–1073, 2012.

[12] M. Lubberink, R. Boellaard, H. N. J. M. Greuter, and A. A. Lammertsma, "Effect of uncertainty in plasma metabolite levels on kinetic analysis of [ 11 C ] flumazenil and [ 11 C ] ( R ) -PK11195 PET studies," *NeuroImage*, vol. 22 Suppl.2, pp. T61–T200, 2004.

[13] R. V. Parsey, A. Ojha, R. T. Ogden, K. Erlandsson, D. Kumar, M. Landgrebe, R. Van Heertum, and J. J. Mann, "Metabolite considerations in the in vivo quantification of serotonin transporters using 11C-DASB and PET in humans," *J Nucl Med*, vol. 47, no. 11, pp. 1796–1802, 2006.

[14] S. Wu, R. T. Ogden, J. J. Mann, and R. V. Parsey, "Optimal metabolite curve fitting for kinetic modeling of 11C-WAY-100635." *Journal of nuclear medicine : official publication, Society of Nuclear Medicine*, vol. 48, no. 6, pp. 926–931, 2007.

[15] H. Watabe, M. a. Channing, M. G. Der, H. R. Adams, E. Jagoda, P. Herscovitch, W. C. Eckelman, and R. E. Carson, "Kinetic analysis of the 5-HT2A ligand [11C]MDL 100,907." *Journal of cerebral blood flow and metabolism : official journal of the International Society of Cerebral Blood Flow and Metabolism*, vol. 20, pp. 899–909, 2000.

[16] P. T. Meyer, D. Elmenhorst, D. Bier, M. H. Holschbach, A. Matusch, H. H. Coenen, K. Zilles, and A. Bauer, "Quantification of cerebral A1 adenosine receptors in humans using [18F]CPFPX and PET: An equilibrium approach," *NeuroImage*, vol. 24, pp. 1192–1204, 2005.

[17] R. Hinz, Z. Bhagwagar, P. J. Cowen, V. J. Cunningham, and P. M. Grasby, "Validation of a tracer kinetic model for the quantification of 5-HT(2A) receptors in human brain with [(11)C]MDL 100,907." *Journal of cerebral blood*

*flow and metabolism : official journal of the International Society of Cerebral Blood Flow and Metabolism*, vol. 27, pp. 161–172, 2007.

[18] R. N. Gunn, P. a. Sargent, C. J. Bench, E. a. Rabiner, S. Osman, V. W. Pike, S. P. Hume, P. M. Grasby, and a. a. Lammertsma, "Tracer kinetic modeling of the 5-HT1A receptor ligand [carbonyl-11C]WAY-100635 for PET." *NeuroImage*, vol. 8, no. 8, pp. 426–440, 1998.

[19] M. Lubberink, G. Luurtsema, B. N. M. van Berckel, R. Boellaard, R. Toornvliet, A. D. Windhorst, E. J. F. Franssen, and A. a. Lammertsma, "Evaluation of tracer kinetic models for quantification of P-glycoprotein function using (R)-[11C]verapamil and PET." *Journal of cerebral blood flow and metabolism : official journal of the International Society of Cerebral Blood Flow and Metabolism*, vol. 27, pp. 424–433, 2007.

[20] U. M. H. Klumpers, D. J. Veltman, R. Boellaard, E. F. Comans, C. Zuketto, M. Yaqub, J. E. M. Mourik, M. Lubberink, W. J. G. Hoogendijk, and A. a. Lammertsma, "Comparison of plasma input and reference tissue models for analysing [(11)C]flumazenil studies." *Journal of cerebral blood flow and metabolism : official journal of the International Society of Cerebral Blood Flow and Metabolism*, vol. 28, pp. 579–587, 2008.

[21] T. G. Lohith, S. S. Zoghbi, C. L. Morse, M. F. Araneta, V. N. Barth, N. a. Goebl, J. T. Tauscher, V. W. Pike, R. B. Innis, and M. Fujita, "Brain and Whole-Body Imaging of Nociceptin/Orphanin FQ Peptide Receptor in Humans Using the PET Ligand 11C-NOP-1A," *Journal of Nuclear Medicine*, vol. 53, pp. 385–392, 2012.

[22] M.-C. Asselin, A. J. Montgomery, P. M. Grasby, and S. P. Hume, "Quantification of PET studies with the very high-affinity dopamine D2/D3 receptor ligand [11C]FLB 457: re-evaluation of the validity of using a cerebellar reference region." *Journal of cerebral blood flow and metabolism : official journal of the International Society of Cerebral Blood Flow and Metabolism*, vol. 27, pp. 378–392, 2007.

[23] P. Edison, D. J. Brooks, F. E. Turkheimer, H. a. Archer, and R. Hinz, "Strategies for the generation of parametric images of [11C]PIB with plasma input functions considering discriminations and reproducibility," *NeuroImage*, vol. 48, no. 2, pp. 329–338, 2009. [Online]. Available: http://dx.doi.org/10.1016/j.neuroimage.2009.06.079

[24] K. B. Contractor, L. M. Kenny, C. R. Coombes, F. E. Turkheimer, E. O. Aboagye, and L. Rosso, "Evaluation of limited blood sampling population input approaches for kinetic quantification of [18F]fluorothymidine PET data," *EJNMMI Research*, vol. 2, no. 1, p. 11, 2012. [Online]. Available: http://www.ejnmmires.com/content/2/1/11

[25] A. Abi-Dargham, N. Simpson, L. Kegeles, R. Parsey, D. R. Hwang, S. Anjilvel, Y. Zea-Ponce, I. Lombardo, R. Van Heertum, J. J. Mann, C. Foged, C. Halldin, and M. Laruelle, "PET studies of binding competition between endogenous dopamine and the D1 radiotracer [11C]NNC 756," *Synapse*, vol. 32, no. July 1998, pp. 93–109, 1999.

[26] Y. Magata, T. Mukai, M. Ihara, S. Nishizawa, H. Kitano, K. Ishizu, H. Saji, and J. Konishi, "Simple analytic method of 11C-flumazenil metabolite in blood." *Journal of nuclear medicine : official publication, Society of Nuclear Medicine*, vol. 44, pp. 417–421, 2003.

[27] M. a. Kropholler, R. Boellaard, A. Schuitemaker, B. N. M. van Berckel, G. Luurtsema, A. D. Windhorst, and A. a. Lammertsma, "Development of a tracer kinetic plasma input model for (R)-[11C]PK11195 brain studies." *Journal of cerebral blood flow and metabolism : official journal of the International Society of Cerebral Blood Flow and Metabolism*, vol. 25, pp. 842–851, 2005.

[28] F. Lamare, R. Hinz, O. Gaemperli, F. Pugliese, J. C. Mason, T. Spinks, P. G. Camici, and O. E. Rimoldi, "Detection and quantification of large-vessel inflammation with 11C-(R)-PK11195 PET/CT." *Journal of nuclear medicine : official publication, Society of Nuclear Medicine*, vol. 52, pp. 33–39, 2011.

[29] R. a. Hawkins, S. C. Huang, J. R. Barrio, R. E. Keen, D. Feng, J. C. Mazziotta, and M. E. Phelps, "Estimation of local cerebral protein synthesis rates with L-[1-11C]leucine and PET: methods, model, and results in animals and humans." *Journal of cerebral blood flow and metabolism : official journal of the International Society of Cerebral Blood Flow and Metabolism*, vol. 9, pp. 446–460, 1989.

[30] M. Naganawa, L. K. Jacobsen, M. Q. Zheng, S. F. Lin, A. Banerjee, W. Byon, D. Weinzimmer, G. Tomasi, N. Nabulsi, S. Grimwood, L. L. Badura, R. E. Carson, T. J. McCarthy, and Y. Huang, "Evaluation of the agonist PET radioligand [11C]GR103545 to image kappa opioid receptor in humans: Kinetic model selection, test-retest reproducibility and receptor occupancy by the antagonist PF-04455242," *NeuroImage*, vol. 99, pp. 69–79, 2014. [Online]. Available: http://dx.doi.org/10.1016/j.neuroimage.2014.05.033

[31] V. Oikonen, "Effect of tracer metabolism during sample preparation," in *XIII Turku PET Symposium*, 2014.

[32] T. G. Lohith, R. Xu, T. Tsujikawa, C. L. Morse, K. B. Anderson, R. L. Gladding, S. S. Zoghbi, M. Fujita, R. B. Innis, and V. W. Pike, "Evaluation in monkey of two candidate PET radioligands, [11C]RX-1 and [18F]RX-2, for imaging brain 5-HT 4 receptors," *Synapse*, vol. 68, no. 12, pp. 613–623, 2014. [Online]. Available: http://doi.wiley.com/10.1002/syn.21773

[33] S. C. Huang, J. R. Barrio, D. C. Yu, B. Chen, S. Grafton, W. P. Melega, J. M. Hoffman, N. Satyamurthy, J. C. Mazziotta, and M. E. Phelps, "Modelling approach for separating blood time-activity curves in positron emission tomographic studies." *Physics in medicine and biology*, vol. 36, no. 6, pp. 749–761, 1991.

[34] R. E. Carson, a. Breier, a. de Bartolomeis, R. C. Saunders, T. P. Su, B. Schmall, M. G. Der, D. Pickar, and W. C. Eckelman, "Quantification of amphetamine-induced changes in [11C]raclopride binding with continuous infusion." *Journal of cerebral blood flow and metabolism : official journal of the International Society of Cerebral Blood Flow and Metabolism*, vol. 17, pp. 437–447, 1997.

[35] R. N. Gunn, S. R. Gunn, and V. J. Cunningham, "Positron emission tomography compartmental models." *Journal of cerebral blood flow and metabolism : official journal of the International Society of Cerebral Blood Flow and Metabolism*, vol. 21, pp. 635–652, 2001.

[36] P. Cumming, G. C. Léger, H. Kuwabara, and A. Gjedde, "Pharmacokinetics of Plasma 6-[18F]Fluoro-L-3,4-dihydroxyphenylalanine[18F]FDOPA in Humans," *Journal of Cerebral Blood Flow & Metabolism*, vol. 13, no. k I, pp. 668–675, 1993.

[37] H. Kuwabara, P. Cumming, J. Reith, G. Léger, M. Diksic, a. C. Evans, and a. Gjedde, "Human striatal L-dopa decarboxylase activity estimated in vivo using 6-[18F]fluoro-dopa and positron emission tomography: error analysis and application to normal subjects." *Journal of cerebral blood flow and metabolism : official journal of the International Society of Cerebral Blood Flow and Metabolism*, vol. 13, pp. 43–56, 1993.

[38] D. a. Mankoff, a. F. Shields, M. M. Graham, J. M. Link, J. F. Eary, and K. a. Krohn, "Kinetic analysis of 2-[carbon-11]thymidine PET imaging studies: compartmental model and mathematical analysis." *Journal of nuclear*

*medicine : official publication, Society of Nuclear Medicine*, vol. 39, pp. 1043–1055, 1998.

[39] T. Tsujikawa, S. S. Zoghbi, J. Hong, S. R. Donohue, K. J. Jenko, R. L. Gladding, C. Halldin, V. W. Pike, R. B. Innis, and M. Fujita, "In vitro and in vivo evaluation of 11C-SD5024, a novel PET radioligand for human brain imaging of cannabinoid CB1 receptors," *NeuroImage*, vol. 84, pp. 733–741, 2014. [Online]. Available: http://dx.doi.org/10.1016/j.neuroimage.2013.09.043

[40] Y. Kimura, K. Ishii, N. Fukumitsu, K. Oda, T. Sasaki, K. Kawamura, and K. Ishiwata, "Quantitative analysis of adenosine A1 receptors in human brain using positron emission tomography and [1 -methyl-11C]8-dicyclopropylmethyl-1-methyl-3-propylxanthine," *Nuclear Medicine and Biology*, vol. 31, pp. 975–981, 2004.

[41] J. Hirvonen, J. Johansson, M. Teras, V. Oikonen, V. Lumme, P. Virsu, A. Roivainen, K. Nagren, C. Halldin, L. Farde, and J. Hietala, "Measurement of striatal and extrastriatal dopamine transporter binding with high-resolution PET and [11C]PE2I: quantitative modeling and test-retest reproducibility." *Journal of cerebral blood flow and metabolism : official journal of the International Society of Cerebral Blood Flow and Metabolism*, vol. 28, pp. 1059–1069, 2008.

[42] M. Yaqub, R. Boellaard, B. N. M. van Berckel, N. Tolboom, G. Luurtsema, A. a. Dijkstra, M. Lubberink, A. D. Windhorst, P. Scheltens, and A. a. Lammertsma, "Evaluation of tracer kinetic models for analysis of [18 F]FDDNP studies," *Molecular Imaging and Biology*, vol. 11, no. April, pp. 322–333, 2009.

[43] C. J. Endres, M. G. Pomper, M. James, O. Uzuner, D. a. Hammoud, C. C. Watkins, A. Reynolds, J. Hilton, R. F. Dannals, and M. Kassiou, "Initial evaluation of 11C-DPA-713, a novel TSPO PET ligand, in humans." *Journal of nuclear medicine : official publication, Society of Nuclear Medicine*, vol. 50, no. 8, pp. 1276–1282, 2009.

[44] A. Jučaite, Z. Cselényi, A. Arvidsson, G. Ahlberg, P. Julin, K. Varnäs, P. Stenkrona, J. Andersson, C. Halldin, and L. Farde, "Kinetic analysis and test-retest variability of the radioligand [11C](R)-PK11195 binding to TSPO in the human brain - a PET study in control subjects," *EJNMMI Research*, vol. 2, p. 15, 2012.

[45] A. Roivainen, K. Nagren, J. Hirvonen, V. Oikonen, P. Virsu, T. Tolvanen, and J. O. Rinne, "Whole-body distribution and metabolism of [N-methyl-11C](R)-1-(2-chlorophenyl)-N-(1-methylpropyl)-3-isoquinolinecarboxamide in humans; an imaging agent for in vivo assessment of peripheral benzodiazepine receptor activity with positron emission tomography," *European journal of nuclear medicine and molecular imaging*, vol. 36, pp. 671–682, 2009.

[46] P. Luoto, S. Suilamo, V. Oikonen, E. Arponen, S. Helin, J. Herttuainen, J. Hietamäki, A. Holopainen, M. Kailajärvi, J. M. Peltonen, J. Rouru, J. Sallinen, M. Scheinin, J. Virta, K. Virtanen, I. Volanen, A. Roivainen, and J. O. Rinne, "11C-ORM-13070, a novel PET ligand for brain $\alpha$2C-adrenoceptors: radiometabolism, plasma pharmacokinetics, whole-body distribution and radiation dosimetry in healthy men," *European Journal of Nuclear Medicine and Molecular Imaging*, vol. 41, no. 10, pp. 1947–1956, 2014. [Online]. Available: http://link.springer.com/10.1007/s00259-014-2782-y

[47] Q. Guo, A. Colasanti, D. R. Owen, M. Onega, A. Kamalakaran, I. Bennacef, P. M. Matthews, E. a. Rabiner, F. E. Turkheimer, and R. N. Gunn, "Quantification of the specific translocator protein signal of 18F-PBR111 in healthy humans: a genetic polymorphism effect on in vivo binding." *Journal of nuclear medicine : official publication, Society of Nuclear Medicine*, vol. 54, pp. 1915–23, 2013. [Online]. Available: http://www.ncbi.nlm.nih.gov/pubmed/24071511

[48] D. R. Owen, Q. Guo, N. J. Kalk, A. Colasanti, D. Kalogiannopoulou, R. Dimber, Y. L. Lewis, V. Libri, J. Barletta, J. Ramada-Magalhaes, A. Kamalakaran, D. J. Nutt, J. Passchier, P. M. Matthews, R. N. Gunn, and E. A. Rabiner, "Determination of [(11)C]PBR28 binding potential in vivo: a first human TSPO blocking study." *Journal of cerebral blood flow and metabolism : official journal of the International Society of Cerebral Blood Flow and Metabolism*, vol. 34, no. 6, pp. 989–94, 6 2014. [Online]. Available: http://www.ncbi.nlm.nih.gov/pubmed/24643083http://www.pubmedcentral.nih.gov/articlerender.fcgi?artid=PMC4050243

[49] C. J. Endres, B. Bencherif, J. Hilton, I. Madar, and J. J. Frost, "Quantification of brain $\mu$-opioid receptors with [11C]carfentanil: Reference-tissue methods," *Nuclear Medicine and Biology*, vol. 30, pp. 177–186, 2003.

[50] M. Tarkia, A. Saraste, T. Saanijoki, V. Oikonen, T. Vähäsilta, M. Strandberg, C. Stark, T. Tolvanen, M. Teräs, T. Savunen, M. a.

Green, J. Knuuti, and A. Roivainen, "Evaluation of 68Ga-labeled tracers for PET imaging of myocardial perfusion in pigs," *Nuclear Medicine and Biology*, vol. 39, no. 5, pp. 715–723, 2012. [Online]. Available: http://dx.doi.org/10.1016/j.nucmedbio.2011.11.007

[51] K. Ishiwata, T. Itou, M. Ohyama, T. Yamada, M. Mishina, K. Ishii, T. Nariai, T. Sasaki, K. Oda, H. Toyama, and M. Senda, "Metabolite analysis of [11C]flumazenil in human plasma: assessment as the standardized value for quantitative PET studies." *Annals of nuclear medicine*, vol. 12, no. 1, pp. 55–9, 2 1998. [Online]. Available: http://www.ncbi.nlm.nih.gov/pubmed/9559964

[52] Y. Ikoma, F. Yasuno, H. Ito, T. Suhara, M. Ota, H. Toyama, Y. Fujimura, A. Takano, J. Maeda, M.-R. Zhang, R. Nakao, and K. Suzuki, "Quantitative analysis for estimating binding potential of the peripheral benzodiazepine receptor with [(11)C]DAA1106." *Journal of cerebral blood flow and metabolism : official journal of the International Society of Cerebral Blood Flow and Metabolism*, vol. 27, pp. 173–184, 2007.

[53] S.-J. Park-Holohan, M.-C. Asselin, D. R. Turton, S. L. Williams, S. P. Hume, P. G. Camici, and O. E. Rimoldi, "Quantification of [11C]GB67 binding to cardiac $\alpha$1-adrenoceptors with positron emission tomography: validation in pigs," *European Journal of Nuclear Medicine and Molecular Imaging*, vol. 35, no. 9, pp. 1624–1635, 2008. [Online]. Available: http://link.springer.com/10.1007/s00259-008-0805-2

[54] M. A. Peyronneau, W. Saba, S. Goutal, A. Damont, F. Dollé, M. Kassiou, M. Bottlaender, and H. Valette, "Metabolism and quantification of [18F]DPA-714, a new TSPO positron emission tomography radioligand," *Drug Metabolism and Disposition*, vol. 41, no. January, pp. 122–131, 2013.

[55] a. a. Lammertsma, C. J. Bench, G. W. Price, J. E. Cremer, S. K. Luthra, D. Turton, N. D. Wood, and R. S. Frackowiak, "Measurement of cerebral monoamine oxidase B activity using L-[11C]deprenyl and dynamic positron emission tomography." *Journal of cerebral blood flow and metabolism : official journal of the International Society of Cerebral Blood Flow and Metabolism*, vol. 11, pp. 545–556, 1991.

[56] a. Buck, H. G. Wolpers, G. D. Hutchins, V. Savas, T. J. Mangner, N. Nguyen, and M. Schwaiger, "Effect of carbon-11-acetate recirculation on estimates of myocardial oxygen consumption by PET." *Journal of nuclear medicine : official publication, Society of Nuclear Medicine*, vol. 32, no. 10, pp. 1950–1957, 1991.

[57] M. T. Wyss, B. Weber, V. Treyer, S. Heer, L. Pellerin, P. J. Magistretti, and A. Buck, "Stimulation-induced increases of astrocytic oxidative metabolism in rats and humans investigated with 1-11C-acetate." *Journal of cerebral blood flow and metabolism : official journal of the International Society of Cerebral Blood Flow and Metabolism*, vol. 29, pp. 44–56, 2009.

[58] A. Hammers, M. C. Asselin, F. E. Turkheimer, R. Hinz, S. Osman, G. Hotton, D. J. Brooks, J. S. Duncan, and M. J. Koepp, "Balancing bias, reliability, noise properties and the need for parametric maps in quantitative ligand PET: [11C]diprenorphine test-retest data," *NeuroImage*, vol. 38, pp. 82–94, 2007.

[59] G. E. Searle, J. D. Beaver, A. Tziortzi, R. a. Comley, M. Bani, G. Ghibellini, E. Merlo-Pich, E. a. Rabiner, M. Laruelle, and R. N. Gunn, "Mathematical modelling of [11C]-(+)-PHNO human competition studies." *NeuroImage*, vol. 68, pp. 119–32, 2013. [Online]. Available: http://www.ncbi.nlm.nih.gov/pubmed/23207573

[60] D. Feng, S. C. Huang, and X. Wang, "Models for computer simulation studies of input functions for tracer kinetic modeling with positron emission tomography," *Int J Biomed Comput*, vol. 32, no. 2, pp. 95–110, 1993.

[61] T. G. Lohith, S. S. Zoghbi, C. L. Morse, M. D. F. Araneta, V. N. Barth, N. a. Goebl, J. T. Tauscher, V. W. Pike, R. B. Innis, and M. Fujita, "Retest imaging of [11C]NOP-1A binding to nociceptin/orphanin FQ peptide (NOP) receptors in the brain of healthy humans," *NeuroImage*, vol. 87, pp. 89–95, 2014. [Online]. Available: http://dx.doi.org/10.1016/j.neuroimage.2013.10.068

[62] G. E. Terry, J.-S. Liow, S. S. Zoghbi, J. Hirvonen, A. G. Farris, A. Lerner, J. T. Tauscher, J. M. Schaus, L. Phebus, C. C. Felder, C. L. Morse, J. S. Hong, V. W. Pike, C. Halldin, and R. B. Innis, "Quantitation of cannabinoid CB1 receptors in healthy human brain using positron emission tomography and an inverse agonist radioligand." *NeuroImage*, vol. 48, no. 2, pp. 362–370, 2009. [Online]. Available: http://dx.doi.org/10.1016/j.neuroimage.2009.06.059

[63] P. Zanotti-Fregonara, S. S. Zoghbi, J. S. Liow, E. Luong, R. Boellaard, R. L. Gladding, V. W. Pike, R. B. Innis, and M. Fujita, "Kinetic analysis in human brain of [11C](R)-rolipram, a positron emission tomographic radioligand to image phosphodiesterase 4: a retest study and use of an image-derived input function," *Neuroimage*, vol. 54, no. 3, pp. 1903–1909, 2011. [Online]. Available: http://dx.doi.org/10.1016/j.neuroimage.2010.10.064

[64] A. Bertoldo, P. Vicini, G. Sambuceti, A. A. Lammertsma, O. Parodi, and C. Cobelli, "Evaluation of compartmental and spectral analysis models of [18F]FDG kinetics for heart and brain studies with PET," *IEEE Transactions on Biomedical Engineering*, vol. 45, no. 12, pp. 1429–1448, 1998.

[65] H. Akaike, "'A new look at the statistical model identification'," *IEEE Transactionson Automatic Control*, vol. 19, no. 6, pp. 716–723, 1974.

[66] R. B. Innis, V. J. Cunningham, J. Delforge, M. Fujita, A. Gjedde, R. N. Gunn, J. Holden, S. Houle, S.-C. Huang, M. Ichise, H. Iida, H. Ito, Y. Kimura, R. a. Koeppe, G. M. Knudsen, J. Knuuti, A. a. Lammertsma, M. Laruelle, J. Logan, R. P. Maguire, M. a. Mintun, E. D. Morris, R. Parsey, J. C. Price, M. Slifstein, V. Sossi, T. Suhara, J. R. Votaw, D. F. Wong, and R. E. Carson, "Consensus nomenclature for in vivo imaging of reversibly binding radioligands." *Journal of cerebral blood flow and metabolism : official journal of the International Society of Cerebral Blood Flow and Metabolism*, vol. 27, pp. 1533–1539, 2007.

[67] B. M. Mazoyer, R. H. Huesman, T. F. Budinger, and B. L. Knittel, "Dynamic PET data analysis." *Journal of computer assisted tomography*, vol. 10, pp. 645–53, 1986. [Online]. Available: http://www.ncbi.nlm.nih.gov/pubmed/3488337

[68] M. Veronese, A. Bertoldo, S. Bishu, A. Unterman, G. Tomasi, C. B. Smith, and K. C. Schmidt, "A spectral analysis approach for determination of regional rates of cerebral protein synthesis with the L-[1-(11)C]leucine PET method," *J Cereb Blood Flow Metab*, vol. 30, no. 8, pp. 1460–1476, 2010. [Online]. Available: http://dx.doi.org/10.1038/jcbfm.2010.26

[69] D. A. Riaño Barros, C. J. McGinnity, L. Rosso, R. A. Heckemann, O. D. Howes, D. J. Brooks, J. S. Duncan, F. E. Turkheimer, M. J. Koepp, and A. Hammers, "Test-retest reproducibility of cannabinoid-receptor type 1 availability quantified with the PET ligand [11C]MePPEP," *NeuroImage*, vol. 97, pp. 151–162, 2014. [Online]. Available: http://dx.doi.org/10.1016/j.neuroimage.2014.04.020

[70] M. Veronese, K. C. Schmidt, C. B. Smith, and A. Bertoldo, "Use of spectral analysis with iterative filter for voxelwise determination of regional rates of cerebral protein synthesis with L-[1-11C]leucine PET." *Journal of cerebral blood flow and metabolism : official journal of the International Society of Cerebral Blood Flow and Metabolism*, vol. 32, no. 6, pp. 1073–85, 6 2012. [Online]. Available: http://www.pubmedcentral.nih.gov/articlerender.fcgi?artid=3367224{&}tool=pmcentrez{&}rendertype=abstract

[71] R. V. Parsey, M. Slifstein, D.-R. R. Hwang, A. Abi-Dargham, N. Simpson, O. Mawlawi, N.-N. N. Guo, R. Van Heertum, J. J. Mann, and M. Laruelle, "Validation and Reproducibility of Measurement of 5-HT1A Receptor Parameters With [carbonyl-11C]WAY-100635 in Humans: Comparison of Arterial and Reference Tissue Input Functions," *Journal of Cerebral Blood Flow and Metabolism*, vol. 20, no. 7, pp. 1111–33, 7 2000. [Online]. Available: http://dx.doi.org/10.1097/00004647-200007000-00011http://www.ncbi.nlm.nih.gov/pubmed/10908045

[72] F. Zanderigo, R. T. Ogden, and R. V. Parsey, "Noninvasive blood-free full quantification of positron emission tomography radioligand binding," *Journal of Cerebral Blood Flow & Metabolism*, vol. 35, no. 1, pp. 148–156, 2014. [Online]. Available: http://www.nature.com/doifinder/10.1038/jcbfm.2014.191

[73] C. S. Hines, M. Fujita, S. S. Zoghbi, J. S. Kim, Z. Quezado, P. Herscovitch, N. Miao, M. D. Ferraris Araneta, C. Morse, V. W. Pike, J. Labovsky, and R. B. Innis, "Propofol Decreases In Vivo Binding of 11C-PBR28 to Translocator Protein (18 kDa) in the Human Brain," *Journal of Nuclear Medicine*, vol. 54, no. 1, pp. 64–69, 2012. [Online]. Available: http://jnm.snmjournals.org/cgi/doi/10.2967/jnumed.112.106872

[74] S. Bishu, K. C. Schmidt, T. Burlin, M. Channing, S. Conant, T. Huang, Z.-h. H. Liu, M. Qin, A. Unterman, Z. Xia, A. Zametkin, P. Herscovitch, and C. B. Smith, "Regional rates of cerebral protein synthesis measured with L-[1-11C]leucine and PET in conscious, young adult men: normal values, variability, and reproducibility," *J Cereb Blood Flow Metab*, vol. 28, no. 8, pp. 1502–1513, 2008. [Online]. Available: http://www.pubmedcentral.nih.gov/articlerender.fcgi?artid=2775471{&}tool=pmcentrez{&}rendertype=abstract

[75] D. P. Devanand, A. Mikhno, G. H. Pelton, K. Cuasay, G. Pradhaban, J. S. Dileep Kumar, N. Upton, R. Lai, R. N. Gunn, V. Libri, X. Liu, R. van Heertum, J. J. Mann, and R. V. Parsey, "Pittsburgh compound B (11C-PIB) and fluorodeoxyglucose (18 F-FDG) PET in patients with Alzheimer disease, mild cognitive impairment, and healthy controls." *Journal of geriatric psychiatry and neurology*, vol. 23, no. 3, pp. 185–98, 9 2010. [Online]. Available: http://www.pubmedcentral.nih.gov/articlerender.fcgi?artid=3110668{&}tool=pmcentrez{&}rendertype=abstract

[76] G. F. Knoll, *Radiation Detection and Measurement*, Wiley, Ed., 2010, vol. 3.

[77] J.-Y. Peng, J. a. D. Aston, R. N. Gunn, C.-Y. Liou, and J. Ashburner, "Dynamic positron emission tomography data-driven analysis using sparse Bayesian learning." *IEEE transactions on medical imaging*, vol. 27, no. 9, pp. 1356–69, 2008. [Online]. Available: http://www.ncbi.nlm.nih.gov/pubmed/18753048

[78] K. Schmidt, "Which linear compartmental systems can be analyzed by spectral analysis of PET output data summed over all compartments?" *J Cereb Blood Flow Metab*, vol. 19, no. 5, pp. 560–569, 1999.

[79] K. P. Wong, S. C. Huang, and M. J. Fulham, "Evaluation of an input function model that incorporates the injection schedule in FDG-PET studies," *IEEE Nuclear Science Symposium Conference Record*, vol. 4, pp. 2086–2090, 2007.

[80] V. M. R. Muggeo, "Estimating regression models with unknown breakpoints," *Statistics in Medicine*, vol. 22, no. 19, pp. 3055–3071, 2003.

[81] M. Tipping, "Sparse Bayesian Learning and the Relevance Vector Mach," *Journal of Machine Learning Research*, vol. 1, pp. 211–244, 2001. [Online]. Available: papers2://publication/uuid/0DF6C0CC-E84B-4734-BD88-2BC0965957E1

[82] R. Tibshirani, "Regression Selection and Shrinkage via the Lasso," pp. 267–288, 1996. [Online]. Available: http://citeseer.ist.psu.edu/viewdoc/summary?doi=10.1.1.35.7574

[83] P. S. Bloomfield, S. Selvaraj, M. Veronese, G. Rizzo, A. Bertoldo, D. R. Owen, M. A. P. Bloomfield, I. Bonoldi, N. Kalk, F. Turkheimer, P. McGuire, V. de Paola, and O. D. Howes, "Microglial Activity in People at Ultra High Risk of Psychosis and in Schizophrenia: An [ 11 C]PBR28 PET Brain Imaging Study," *American Journal of Psychiatry*, vol. 173, no. 1, p. appi.ajp.2015.1, 10 2015. [Online]. Available: http://www.ncbi.nlm.nih.gov/pubmed/26472628http://www.pubmedcentral.nih.gov/articlerender.fcgi?artid=PMC4821370

[84] G. Rizzo, M. Veronese, M. Tonietto, P. Zanotti-Fregonara, F. E. Turkheimer, and A. Bertoldo, "Kinetic modeling without accounting for the vascular component impairs the quantification of [11C]PBR28 brain PET data," *Journal of Cerebral Blood Flow & Metabolism*, vol. 34, no. 6, pp. 1060–1069, 6 2014. [Online]. Available: http://www.ncbi.nlm.nih.gov/pubmed/24667911http://www.nature.com/doifinder/10.1038/jcbfm.2014.55

[85] H. Ku, "Notes on the use of propagation of error formulas," *Journal of Research of the National Bureau of Standards, Section C: Engineering and Instrumentation*, vol. 70C, no. 4, p. 263, 1966. [Online]. Available: http://nvlpubs.nist.gov/nistpubs/jres/70C/jresv70Cn4p263{_}A1b.pdf